Revision 1

Crystal versus melt compositional effects on the partitioning of the first-row transition and high field strength elements between clinopyroxene and silicic, alkaline, aluminous melts

Zhiwei He[a,b,*], Yuan Li[c], Zhenhui Hou[a,d], Fang Huang[a,d,*]

[a]*School of Earth and Space Sciences, University of Science & Technology of China, Hefei, Anhui 230026, China*

[b]*State Key Laboratory of Marine Geology, Tongji University, Shanghai 200092, China*

[c]*State Key Laboratory of Isotope Geochemistry, Guangzhou Institute of Geochemistry, Chinese Academy of Sciences, Guangzhou 510640, China*

[d]*CAS Center for Excellence in Comparative Planetology, University of Science & Technology of China, Hefei, Anhui 230026, China*

Abstract word count: 453

Text words: ~7769

Figure#: 10

Table#: 4

References# 95

*Corresponding authors:

E-mail address: fhuang@ustc.edu.cn (F. Huang) and hezw@tongji.edu.cn (Z.W. He)

Abstract

The first-row transition element (FRTE) and high field strength element (HFSE) systematics are powerful tools for tracking the source and evolution of mantle-derived magmas. Clinopyroxene is generally considered a key fractionating mineral controlling the partitioning of trace elements between melt and residual solid during mantle melting. Although partitioning of FRTE and HFSE between clinopyroxene and basaltic melts has been well studied, experimental constraints on their partitioning behaviors in the presence of siliceous, aluminous and alkali-rich melts are still lacking. Here we present clinopyroxene-silicic melt (67–69 wt% SiO_2) partitioning experiments at 1 bar pressure and 1070–1100 °C for Co, Mn, Ni, Cu, Zn, Fe, Sc, Cr, V, Ti, Zr, Hf, Nb, and Ta. Run products consist of diopsidic clinopyroxene coexisting with various melt compositions with non-bridging oxygen to tetrahedral cation ratio (NBO/T) ranging from 0.10 to 0.22. Using our new partition coefficients (*D*s) and combining literature data we assess some of the effects of crystal chemistry and the melt composition on the partitioning of FRTE and HFSE in this simple system.

We show that partitioning of FRTE varies from mildly incompatible (e.g., D = ~0.1−1 for V, Cu, and Zn) to highly compatible (e.g., $D > 10$ for Cr and Ni), with highest compatibilities observed for Ni (D_{Ni} = 13−34). The partitioning of HFSE varies from highly incompatible (D = 0.01−0.08) for Nb and Ta to mildly incompatible (D = 0.18−0.82) for Zr, Hf, and Ti. Our measured clinopyroxene-melt *D*s are consistent with the theoretical predictions of the lattice strain model. *D*s data for most tri-, tetra-, and pentavalent elements tend to increase with increasing tetrahedrally-coordinated Al

content, in agreement with those anticipated from crystal-chemical considerations. In contrast to ^{iv}Al, clinopyroxene Na content has very little effect on trace element partitioning due to its insufficient incorporation into clinopyroxene at relatively low-pressure conditions. These data further support a significant control of melt composition/structure on partitioning for highly polymerized melts. In general, measured *D*s roughly increase to different extent with increasing polymerization of the melt (i.e., lower NBO/T or higher ASI). For our equilibrium melt compositions, *D*s for several FRTE such as Co and Ni correlate well with the melt molar $Mg^{2+}/(M^{+} + M^{2+})$ whereas *D*s for FRTE vary as a function of the melt alkalis. These well-defined trends support the role of melt NBO species (e.g., Mg^{2+}) or complexing ligands (e.g., Na^{+} and K^{+}) in controlling the partitioning of these elements.

Overall, our new *D*s data demonstrate that even very small changes in melt major-element compositions can greatly affect element partitioning in strongly polymerized silicic systems. These findings have important implications relevant to petrogenetic studies of the interaction between silicic melt and peridotite that occurs at shallow mantle conditions in a variety of tectonic settings.

Key words: clinopyroxene, melt composition, FRTE, HFSE, partition coefficient

1. Introduction

Siliceous, alkali-rich and aluminous glasses have been widely reported in mantle-derived spinel peridotite xenoliths from a variety of geographic and tectonic localities (e.g., Xu et al., 1996; Vannucci et al., 1998; Yaxley and Kamenetsky, 1999; Miller et al., 2012), including continental alkali basalt provinces, oceanic hot spots, and subduction-related settings. The glasses contain from 40 to >70 wt% SiO_2, up to 17 wt% total alkalies, and up to 25 wt% Al_2O_3 (Yaxley and Kamenetsky, 1999). As a result, the interaction between peridotite and such silicic melts has received considerable attention as an effective mechanism of mantle metasomatism (e.g., Coltorti et al., 2000; Qian et al., 2015), which may contribute to the heterogeneous enrichment of erupted lavas. In particular, phase-equilibria experiments further show that these kinds of melts can be readily in equilibrium with harzburgitic or lherzolitic mineral assemblages at low pressure (Draper and Green, 1997, 1999). Knowledge of element partitioning between mantle minerals and silicic, alkaline, aluminous melts is therefore pivotal to understanding upper mantle processes such as equilibrium partial melting and metasomatism.

Clinopyroxene (cpx) is a common mineral in upper mantle and magmatic rocks that can significantly control the partitioning of trace elements between melt and surrounding solid matrix (e.g., Lundstrom et al., 1994; Wood and Trigila, 2001; Sun and Liang, 2013; Bédard, 2014; Li, 2018; Beard et al., 2019; Ma and Shaw, 2021). Thus, cpx–melt trace element partition coefficients ($D^{cpx/melt}$) are key for interpreting the geochemical characteristics of the silicic melt and ambient mantle peridotite involved

in the interactions. Previous studies investigating cpx–melt partitioning largely focus on mafic to ultramafic systems (e.g., Gaetani and Grove, 1995; Blundy et al., 1998; Lundstrom et al., 1998; Hill et al., 2000; Bonechi et al., 2021), with an emphasis on the importance of crystal-chemical control on trace element partitioning in basaltic melts. For example, a number of experimental studies demonstrated the dependence of rare earth element (REE) and high field strength element (HFSE) partitioning on the abundance of tetrahedral Al (^{iv}Al) or Ca-Tschermakite content in cpx (e.g., Gaetani and Grove, 1995; Hill et al., 2000). As a consequence, most existing theoretical frameworks treat the crystal composition as the dominant role in determining cpx–melt partitioning behavior (e.g., Wood and Blundy, 1997; Sun and Liang, 2012, 2013; Mollo et al., 2018), while the potential influence of the corresponding melt is less considered.

The effects of melt composition/structure on trace element partitioning have been investigated by using coexisting immiscible silicate melts (Watson, 1976; Ryerson and Hess, 1978; Schmidt et al., 2006) or through mineral–melt equilibrium approaches (e.g., Gaetani, 2004; Prowatke and Klemme, 2005; Huang et al., 2006; Miller et al., 2006; Evans et al., 2008; Qian et al., 2015; Michely et al., 2017; Schoneveld and O'Neill, 2019). The pioneering studies of Watson (1976) and Ryerson and Hess (1978) experimentally demonstrated that depolymerized melts preferentially accommodate cations with a high charge density (i.e., high charge/cation radius) such as transition metals, REE, and HFSE, whereas low-charge-density cations such as Cs are better hosted in polymerized melts. Mineral-melt partitioning studies have shown that melt composition/structure effects dominate trace element partitioning when the degree of

melt polymerization exceeds a threshold value (Gaetani, 2004; Mysen, 2004). Consistent with this notion, partition coefficients between minerals and melts for REE could increase by an order of magnitude when the melt changes from basaltic to granitic composition (e.g., Tiepolo et al., 2007; Bédard, 2014).

Despite the potential role of melt compositional variations in controlling crystal–melt partitioning, only a few experimental studies have been conducted to determine the cpx–melt partition coefficients in highly silicic systems (Klein et al., 2000; Huang et al., 2006). This is primarily due to the difficulty in growing large cpx crystals and achieving equilibrium partitioning in high-SiO_2 melts. Although Klein et al. (2000) reported D_{REE} and D_{HFSE} between cpx and andesitic to granodioritic melts, the wide temperature range (900–1150 °C) makes it difficult to identify and quantify the compositional effects. Huang et al. (2006) investigated the effect of melt composition on trace element partitioning between cpx and silicic melts; however, *D*s were only determined for a limited number of trace elements (e.g., REE, Ti, Zr, and Sr). So far there is still a lack of data for showing the crystal versus melt compositional effects on the partitioning behavior of geochemically important trace elements, such as the first-row transition element (FRTE) and HFSE, between cpx and silicic melt.

Accordingly, in this study, we present new partition coefficient data derived from synthetic cpx in equilibrium with anhydrous Si-rich melts whose composition is typical of silicic xenolith glasses reported in the literature (Vannucci et al., 1998). Experiments were conducted by using Pt-crucibles in a high-temperature furnace, at temperatures of 1070–1100 °C, and at atmospheric pressure and oxygen fugacity conditions.

Specifically, we carried out experiments by changing Na_2O content in the system CaO–MgO–Al_2O_3–SiO_2–Na_2O–(K_2O)–Fe_2O_3–TiO_2 to cover a large compositional range such as in natural systems. Since sodium is known to play a significant role in changing cpx crystal chemistry and the structure of silicate melts (e.g., Bennett et al., 2004; Michely et al., 2017; Beard et al., 2019), these measurements enable an assessment of the effect of Na on cpx–melt partitioning. Indeed, rapid diffusive infiltration of sodium into partially molten peridotite is considered as an effective mechanism to account for the creation of silica-rich glasses in mantle xenoliths (Lundstrom 2000).

Our new results, particularly when combined to literature data, clearly show that trace element partitioning in silicic melts differ from those in basaltic melts, and we present a scheme for evaluating the specific influence of different crystal and melt compositional variables on the partitioning of FRTE and HFSE. The data presented in this study thus have important implications for the partitioning behavior of trace elements in evolved silicic systems, particularly for trace element systematics relevant to mantle partial melting or metasomatic processes operated by highly silicic melts.

2. Experimental and analytical methods

2.1. Starting materials

Compositions of the starting materials are presented in Table 1 and their utilization in each experiment is presented in Table S1. As a base starting material, all runs utilized a silicic melt similar in composition to sample HISIL of Huang et al. (2006), based on a glass composition in a harzburgite xenolith from the Canary Islands (Vannucci et al.

153 1998). The starting material HISILA is a synthetic powder, made to correspond to
154 coexisting silica-rich glass (90% by mass) and chromian diopside (10%) in a
155 harzburgite xenolith (PAT2-68; Vannucci et al. 1998). The HISILB has a major element
156 composition similar to that of HISILA but with K_2O replaced by Na_2O. This Na-rich
157 HISILB with ~ 9 wt% Na_2O content was designed to isolate the effect of sodium on the
158 cpx–melt partitioning of trace elements. An additional composition, HISILC, has the
159 same major element concentration as HISILB but is doped with different levels of
160 minor and trace elements. Benefiting from seeding a few large crystals, two
161 experiments were run with HISILA plus a proportion of diopside powder (4–8 wt%),
162 namely HISILA4D and HISILA8D.

163 The starting compositions were chosen on the basis of several criteria: (i)
164 composition HISILA has been studied both in nature and experiments such that phase
165 relations are well constrained (Vannucci et al. 1998; Huang et al., 2006), ensuring the
166 crystallization of cpx in equilibrium with a high proportion of quenched melt; (ii) cpx
167 crystallizes at nearly constant equilibrium conditions, preventing complications in the
168 interpretation of results stemming from the P–T–fO_2 effects; (iii) the liquids produced
169 cover a range of compositions, sufficient for defining the melt compositional
170 dependence of partitioning.

171 The starting materials were synthesized by mixing reagent-grade oxides (SiO_2,
172 Al_2O_3, MgO, and TiO_2) and carbonates ($CaCO_3$, Na_2CO_3, and K_2CO_3). FeO was added
173 as a mixture of high-purity Fe and Fe_2O_3 powders. After an initial grinding of 30 min
174 in an agate mortar in ethanol, the mixtures were dried and placed in a platinum crucible

to decarbonate in a 1 atm furnace at 800 °C overnight, and then fused at 1450 °C for 2 h. The quenched melt was re-ground in ethanol for 3 h and dried again. Selected trace elements (Rb, Sr, Sc, V, Cr, Mn, Co, Ni, Cu, Zn, Zr, Hf, Nb, Ta, La, Ce, Nd, Sm, Eu, Gd, Tb, Dy, Ho, Er, Yb, Lu) were then added to the starting mixture as oxides or nitrate/chloride solutions in an amount of totaling ~0.88 wt%, resulting in individual trace element concentrations of ~100 to 500 ppm (Table S2). The mixture with dopants was ground and heated to 1450 °C for 2 h, and then quenched in cool water. Analyses of the silicate glass confirmed its chemical homogeneity. The produced glass was re-ground and stored for subsequent experiments.

2.2. One-atmosphere experiments

A series of partitioning experiments were conducted by using Pt-crucibles in a high-temperature furnace. Run conditions were anhydrous and atmospheric with regard to pressure (1 atm) and oxygen fugacity (i.e., around $\log f\mathrm{O_2} = -0.7$). The experimental set-up was chosen, in part because silica- and alkali-rich liquids, preserved as glass inclusions in spinel peridotite xenoliths, are mostly restricted to the shallowest (< 45 km) part of the mantle (Hirschmann et al., 1998). Thus, experiments were designed to simulate the equilibration of silicic melts with cpx in close to the upper mantle conditions at low pressure.

In order to maximize crystal size and ensure equilibration of the growing crystals and melt, we implemented a cycled time-temperature path over the course of the study (Table S3; Fig. S1). In detail, the experiments were initially heated to super liquidus temperatures (1300–1450 °C) for 0.5–2 h to ensure complete melting of the powders

and chemical homogenization prior to crystallization. Runs were then cooled and maintained at 1150 °C, above the liquidus (1125 °C), for 2–3 h. Subsequently, runs were oscillated between 1130 °C and the target equilibrium temperatures (1070–1100 °C) with a slow cooling rate of 6–7.2 °C/h and a rapid heating rate of 90–200 °C/h, and the experiments were held at the equilibrium temperature for 5–10 h between oscillations. After several rounds of temperature cycle, runs were decreased to the final equilibrium temperature at rate of around 1 °C/h and maintained for 40–100 h to enhance crystal growth. A part of run products derived from HISILA, HISILB, HISILC, HISILA4D, and HISILA8D compositions was re-used as new starting materials for subsequent runs (Table S1). This experimental approach can create equilibrium cpx–melt pairs with a wide range of melt compositions and the crystalline precursors can serve as a nucleation point for crystals. At the temperature and atmospheric conditions of our experiments, no significant loss of Fe and Na from the melt is expected, as confirmed by electron microprobe analyses of the final fused glasses. All experiments were quenched by quickly dropping the Pt-crucibles into cool water. The recovered samples were then mounted in epoxy resin and polished for chemical analysis. A summary of the experimental conditions is given in Table S1.

2.3. EPMA analysis

Cpx and quenched glasses were analyzed for the major and minor element contents (Si, Al, Fe, Mg, Ca, Na, K, Ti, Cr, Mn, and Ni) by using a JEOL JXA-8100 electron probe micro-analyzer (EPMA) at the State Key Laboratory of Isotope Geochemistry, Guangzhou Institute of Geochemistry, Chinese Academy of Sciences (CAS). The

219 analytical conditions were an acceleration voltage of 15 kV, a beam current of 20 nA,
220 and a defocused beam of 1 μm. Peak counting time was as follows: 10 s for Na and K;
221 20 s for Si, Al, Mg, Ca, and Fe; and 40 s for minor elements. Calibration was performed
222 by using the following natural and synthetic reference materials: chrome diopside (Si,
223 Mg, and Ca), almandine (Fe and Al), albite (Na), orthoclase (K), Cr_2O_3 (Cr), rutile (Ti),
224 and MnO (Mn). Data reduction was performed by using the ZAF correction program.
225 The reproducibility and accuracy of the measurements were verified by using a set of
226 secondary standards, which agree well with the recommended values (Table S4).
227 Analytical precision is typically < 1% RSD for Si and < 5% RSD for analytes with
228 concentrations > 0.5 wt%.

229 ## 2.4. LA-ICP-MS analysis

230 Major and trace element analyses of cpx and glasses were performed by LA-ICP-
231 MS using either a GeolasPro 193 nm ArF excimer laser system attached to an Agilent
232 7700e ICP-MS at the CAS Key Laboratory of Crust–Mantle Materials and
233 Environments, University of Science and Technology of China, or a Photon Machines
234 Excite 193 nm ArF excimer laser attached to an Agilent 7700x ICP-MS at the Nanjing
235 FocuMS Technology Co. Ltd. Both instruments employ custom-built, fast-washout
236 sample cells and use He as the sample chamber carrier gas (Hou et al., 2020). In both
237 cases, the instrumental operating parameters were optimized by ablating NIST SRM
238 610 to obtain maximum signal intensity for ^{238}U, while keeping the ThO^+/Th^+ ratio
239 below 0.5% and the U^+/Th^+ ratio close to 1.

240 The sequence of analysis began with four analyses of reference glasses (NIST

241 SRM 610, BHVO-2G, BCR-2G and BIR-1G), followed by analyses of samples and
242 then four analyses of reference glasses again. NIST SRM 610 was repetitively analyzed
243 every eight sample analyses for time-drift correction. Each individual analysis included
244 a background acquisition of the first 30 s (gas blank) followed by 40 s for ablation and
245 then 35 s for gas flow washing. We used a beam size of 30 μm under single-spot mode
246 for glasses while a beam size ranging between 10 and 20 μm under single-spot or line
247 scanning mode for cpx. Though the use of small beam size for cpx may reduce the
248 analyte sensitivity, this problem was largely counteracted due to the high doping levels
249 of the starting mixes (Table S2). For cpx analysis, only laser signals free of melt
250 inclusions and spikes were integrated to yield the elemental concentration.

251 We applied the calibration strategy of summed metal oxide normalization for data
252 reduction (Halicz and Günther 2004, Guillong et al. 2005, Liu et al. 2008), in which the
253 sum of all metal oxides is normalized to 100% m/m. Three USGS glass reference
254 materials (BHVO-2G, BCR-2G, and BIR-1G) were used for external standardization
255 (He et al., 2016), which would provide more precise and accurate elemental
256 concentrations relative to calibration by NIST SRM 610 (Liu et al. 2008). Off-line
257 selection and integration of background and ablation signals, and time-drift correction
258 and quantitative calibration were performed by ICPMSDataCal software (Liu et al.
259 2008). Compared with previous calibration applying internal standardization, this
260 method is able to obtain major and trace element contents simultaneously without an
261 internal standard element pre-determined by EPMA.

262 The anticipated measurement precision (measured as relative standard deviation)

and accuracy (expressed as relative deviation from the reference value) for silicate glasses of this calibration method are better than 5% for major elements and 5–10% for trace elements, based on analyses of USGS and MPI-DING reference glasses (Liu et al. 2008; He et al., 2016). To assess the accuracy of cpx analyses, we also used USGS, MPI-DING, and CGSG glasses as secondary standards. Under these operating conditions, at beam sizes equal or smaller than 20 μm, precision and accuracy typically remain better than 10–20% for most elements (Table S5).

3. Results

3.1. Run products

All experiments produced cpx crystals with the coexisting melt quenched into glass and no other phases present (Table S1). Figure 1 shows the back-scattered electron (BSE) images of two representative cpx crystals from runs 5H05-1 and 9H07-2. Cpx crystals are generally euhedral/subhedral and blade shaped without zoning (Fig. 1), ranging from 10 to 50 μm in the narrowest dimension, with the largest cpx found in the melts of the HISILB/ HISILC composition. Based on optical inspection the modal proportions of cpx crystals are generally < 20%, whereas the quenched melts are clear glasses without any dendritic quench texture (Fig. 1).

3.2. Major element compositions of the silicate glass and cpx

Glass. The major element composition of the run product glasses from LA-ICP-MS analyses is summarized in Table 2. The glasses in all runs are homogenous in

chemistry as illustrated by the small standard deviations in major element analyses (Table 2). On a total-alkalis vs. silica diagram the glasses are predominantly trachydacitic in composition, ranging from 8.8 to 9.7 wt% in total alkali ($Na_2O + K_2O$) content and from 67.6 to 69.1 wt% in the SiO_2 content, resembling the silicic glass observed in a harzburgite xenolith (PAT2-68) from Vannucci et al. (1998). The glasses are also characterized by high Al_2O_3 (14.10–15.51 wt%), and low MgO (1.35–2.56 wt%), FeO_t (1.54–2.11 wt%), TiO_2 (0.11–0.2 wt%) and CaO (1.81–3.18 wt%). Their alumina saturation index (ASI: molar ratio $Al_2O_3/(Na_2O + K2O + CaO)$) is 0.66 to 0.89, resulting in a range of compositions from metaluminous to peralkaline, and the Mg#s (= 100 × Mg/(Mg + Fe) in molar fraction) of these glasses range from 60.1 to 74. The degree of polymerization can be described by the NBO/T parameter (the number of non-bridging oxygens per tetrahedral cation; Mysen and Virgo, 1980), which ranges from 0.10 to 0.22 in our experiments (Table 2).

Cpx. The major element composition of the run product cpx from EPMA analyses is summarized in Table 3. Cpx is also homogeneous in a single run but its composition slightly varies with changes of experimental starting composition and conditions (Table 3). Cpx is Ca- and Mg-rich (21.16–23.3 wt% CaO;17.34–18.5 wt% MgO) but Al-poor (1.7–3.1 wt%) and contains 0.49–0.95 wt% Na_2O. In general, all Fe (1.89–2.61 wt% FeO_t) is assumed to be present as ferric iron in cpx based on the high oxygen fugacity during the runs. For reference, cpx compositions are reported in cations and end-member mole fractions on a six-oxygen basis in Table S6. All cpx crystals produced in these experiments are diopside (Di74−88) in composition with relatively low aegirine

306 (Ae0−5) and enstatite (En1−12) components, whereas their Mg#s range from 92.5 to
307 94.2. The produced cpx in this study therefore resembles the typical diopside coexisting
308 with silicic melts in mantle xenoliths (Vannucci et al., 1998), in terms of high SiO_2,
309 CaO, MgO, and low Al_2O_3 contents.

310 3.3. Cpx–melt partition coefficients

311 Partition coefficients in each experimental run, calculated from LA-ICP-MS or
312 EPMA analyses of cpx–glass pairs (Tables 2–3, S7–S8), are summarized in Table 4.
313 All partition coefficients are reported with 1σ errors calculated by propagating the
314 uncertainties (relative standard deviation) on the concentrations in each phase: $\sigma_D =$
315 $D^{cpx/melt} \times \sqrt{\mathrm{RSD}^2_{Ccpx} + \mathrm{RSD}^2_{Cmelt}}$. Both concentrations and partition coefficients for
316 Ni, Cr, Fe, and Ti by the two analytical methods agree within errors and show no
317 systematic bias (Fig. 2), except for Mn. Reasons for the slight offset in Mn data from
318 the 1:1 line in Fig. 2 most likely arise from the analytical limit for low-concentration
319 elements by EPMA, and in this case, D_{Mn} were calculated based on LA-ICP-MS
320 analyses of cpx. The partition coefficients for LILE and REE from nine representative
321 runs, together with literature data, are depicted in Fig. S2. As expected, both Na and Sr
322 are incompatible in cpx. Notably, D_{Sr} (0.16–0.33) compare well with the range reported
323 by Huang et al. (2006) and those determined from silica-rich glass-diopside pairs in
324 mantle xenoliths (Vannucci et al. 1998), but are elevated relative to typical cpx–basalt
325 values (e.g., 0.089–0.115 in Lundstrom et al., 1994). The REE show a gradual increase
326 in compatibility from light REE (e.g., D_{La} = 0.26–0.4) to middle–heavy REE (e.g., D_{Yb}
327 = 1.27–2.27), with a maximum occurring in the middle REE, typically Dy. This REE

partitioning pattern is in excellent agreement with previous results experimentally measured in silicic system by Huang et al. (2006) while is much higher than those between cpx and basaltic or andesitic melts (e.g., Hart and Dunn, 1993; Skulski et al., 1994; Hill et al., 2000). Because the cpx-silicic melt partitioning for LILE and REE has been fully addressed (Huang et al., 2006), we focus here on FRTE and HFSE partitioning behavior.

A comparison of our measured FRTE and HFSE partition coefficients from nine representative runs with those from the literature is shown in Fig. 3. To the first order, the trends in measured D_{FRTE} and D_{HFSE} are similar among experiments. Most FRTE (i.e., Mn, Co, Ni, Sc, and Cr) are moderately to highly compatible in cpx, with Ni being the most compatible element. Cu and Zn are in general incompatible, with D values between 0.1 and 1. As regards the multivalent transition metals, Fe is slightly compatible in cpx whereas V behaves incompatibly and exhibits the lowest D values (0.06–0.14). Our D_V values are considerably lower than most other experimental partitioning studies (e.g., Toplis and Corgne, 2002; Mallmann and O'Neill, 2009; Li, 2018; Holycross and Cottrell, 2022). The difference is likely due to the higher oxygen fugacity (fO_2) in the system of this study, resulting in elevated V oxidation states (predominantly V^{5+}). Overall, the compatibility of the FRTE increases in the order V < Cu < Zn < Fe < Mn < Co < Sc < Cr < Ni (Fig. 3). With respect to HFSE, the Ds vary from highly incompatible for Nb and Ta and to mildly incompatible for Zr, Hf, and Ti (Fig. 3). For comparison, the FRTE and HFSE partition coefficients obtained here are generally above or at the high end of the literature data associated with basalts (Fig. 3).

Finally, at the run conditions, the limited equilibrium temperature (1070 to 1100 °C) range exerts no obvious influence on *D* values for FRTE and HFSE (Fig. S3).

3.4. Equilibrium partitioning and Henry's law behavior

Several lines of evidence support the attainment of chemical equilibrium during the experiments. First, run durations were much longer than those of previous studies that reached equilibrium (e.g., Hart and Dunn, 1993; Hill et al., 2000; Bennett et al., 2004). Second, major and trace element compositions of cpx and melt phase in each run were found to be widely homogeneous with standard deviations usually in the range of 10% RSD or below (Tables 2–3; Tables S7–S8). To be more specific, EPMA analyses of core–rim transect across the cpx grain revealed no major or minor element zonation (Fig. 4a; Table S9), especially for slow diffusing cations, Al^{3+} and Ti^{4+}, indicating steady state cpx growth without the development of a diffusive boundary layer (Holycross and Watson 2016; 2018). Moreover, the random analyses of major element in glass also revealed no detectable variations outside of analytical errors (Fig. 4b; Table S9). Third, the partition coefficients for K in our experiments (0.01–0.015) are close to those previously reported (e.g., 0.015–0.045 in Johnson, 1998), precluding the enrichment in highly incompatible elements due to fast non-equilibrium growth (Huang et al., 2006). Finally, the *D*s for most investigated trace elements can be well described by the crystal lattice strain model, indicating that our measured partition coefficients represent equilibrium values.

Henry's law behavior of element partitioning between cpx and melt in our experiments is assumed for the following reasons. First, the total dopant levels (<0.9

wt%) in the starting material utilized in this study as well as the element concentrations measured in the run products (Tables S2, S8) are well below the anticipated upper limits of Henrian behavior (Watson, 1985). Second, the experiments with HISILB/HISILC as starting materials show comparable trace element *D*s under the same experimental conditions (e.g., runs 6H05-2 and 7H05-3; see Table 4), despite the fact that the dopants for trace elements are different. Therefore, cpx–melt partitioning in our experiments should obey Henry's law.

4. Discussion

4.1. Lattice strain model

The lattice strain model (LSM) has been widely applied to trace element partitioning between minerals and melt over the last few decades (e.g., Brice, 1975; Blundy and Wood, 1994; Wood and Blundy, 1997; Mollo et al., 2020). In general, the partitioning of isovalent elements into the same crystallographic site of a mineral always shows a near-parabolic dependence on the ionic radii (e.g., an Onuma diagram; Onuma et al., 1968), which can be quantitatively described by the lattice strain equation (Blundy and Wood 1994) as follows:

$$D_i = D_0 * \exp\left(\frac{-4\pi E N_A}{\mathrm{RT}}\left(\frac{r_0}{2}\left(r_i - r_0\right)^2 + \frac{1}{3}\left(r_i - r_0\right)^3\right)\right) \quad (1)$$

where D_i is the partition coefficient of element *i* with ionic radius r_i, D_0 is the partition coefficient for the strain-free substitution, r_0 is the optimum ionic radius of the strain-

free lattice site, E is the apparent Young's modulus (GPa) of the lattice site, R is the universal gas constant (=8.31 J/mol/K), N_A is Avogadro's number, and T is temperature in Kelvin. Of these lattice terms, D_0 and r_0 define the apex location of a parabola on a plot of D_i vs. ionic radius. The apparent Young's modulus E determines the width of the parabola, which reflects the elastic response of the crystallographic site to lattice strain due to the incorporation of elements of non-ideal size (Blundy and Wood, 2003).

In cpx, the sixfold coordinated M1 site incorporates most transition elements and HFSE, including divalent (Co, Ni), trivalent (Cr, Sc), tetravalent (Ti, Zr, Hf), and pentavalent (V, Nb, Ta) cations, whereas the eightfold coordinated M2 site preferentially incorporates the larger cations like monovalent Na, K, and Rb, divalent Ca, Mn, Sr, and Ba, trivalent REE, and tetravalent U and Th (e.g., Blundy and Wood 1994, 2003; Hill et al. 2000). The LSM was applied to our Ds by a non-linear weighted least-squares regression using Eq. (1), which calculates the best-fit values of the lattice strain parameters (r_0, D_0, and E) for both M-sites in cpx. In presence of a low number of measured D for isovalent elements entering the same site, it failed to constrain the lattice strain parameters in regression analysis. Therefore, we choose to fit only the D_0 and E parameters, whereas r_0 for each experiment is fixed in a reasonable range depending on the valence of the trace elements (Dalou et al., 2018). The resultant parabolas of D vs. ionic radius derived from two individual experiments are shown in Fig. 5 (remaining experiments are shown in Fig. S4), and the fitting parameters are listed in Table S10. These lattice strain parabolas thus enable us to assess the quality of the fit of the experimentally determined D values to the LSM. Parabola fits for di-, tri-,

tetra-, and pentavalent elements are described below.

For cations entering the M1 site, the fits of the experimental partitioning data for divalent (Co^{2+}, Ni^{2+}, Mg^{2+}, and Zn^{2+}), trivalent (Al^{3+}, Cr^{3+}, and Sc^{3+}), tetravalent (Ti^{4+}, Zr^{4+}, and Hf^{4+}), and pentavalent (V^{5+}, Nb^{5+}, and Ta^{5+}) cations form distinct parabolas (Fig. 5). Though parabolas for HFSE and 3+ cations on the M1 site are defined by just three elements they are in excellent agreement with the experimentally determined values for all experiments. Note the very few cations that fall off the parabola in some cases are Cu^{2+} and Fe^{3+}, which may be due to analytical uncertainties or the crystal-field effects associated with the mineral-melt partitioning of transition metals (e.g., Mn, Co, Ni, Cu, Fe, Cr, and V; Blundy and Wood, 1994; Cartier et al., 2014).

Consistent with previous studies (e.g., Hill et al., 2000; Dygert et al., 2014; Bonechi et al., 2021), we observe a higher Young's modulus and hence tighter parabola on the M1 site with respect to M2 site (Fig. 5; Table S10). Notably, the high effective Young's moduli for 3+ cations (1554–2100 GPa) obtained on the M1 site is overall close to the measured value for diopsidic cpx (1635 GPa; Hill et al., 2000). The inferred values for E^{4+} (~1147–2472 GPa) from Ti-Hf-Zr regression are also consistent with the large values calculated in previous studies (~800–2400 GPa; Lundstrom et al., 1998; Hill et al., 2011; Baudouin et al., 2020). These observations are accounted for by the elastic properties of the lattice site in which the M1 site is stiffer than the M2 site in cpx (Hill et al., 2011).

The larger divalent cation Mn^{2+} prefers the M2 site along with Ca^{2+} and Sr^{2+} and they define parabolas of wider shape, which yield D_0 of 8–15, r_0 of 1.068–1.086 Å, and

438 E of 268–304, respectively. Among these divalent cations, Ca^{2+} is the cation closer to
439 the apex of parabolas and Mn is more compatible than Sr. It is also clear in Fig. 5 that
440 the parabolas for trivalent elements on the M2 site match well with our experimentally
441 determined D_{REE} values. Lattice strain parameters for REE partitioning are D_0 = 1.58–
442 2.41, r_0 = 1.021–1.038 Å, E = 235–365, consistent with the range (D_0 = 1.09–3.62, r_0
443 = 1.006–1.041, E = 255–366) experimentally obtained in silicic systems (Huang et al.,
444 2006).

445 4.2. Effect of crystal chemistry on D_{FRTE} and D_{HFSE}

446 In general, element partitioning between minerals and melts depends on both
447 crystal chemistry and the melt composition. Although our original intention was to
448 isolate the effect of sodium, the cpx composition of these experiments shows more
449 differences than simply Na content. The melt composition is also considerably different
450 among experiments. Therefore, it presents a challenge in determining the effect of any
451 single compositional parameter independently. However, an advantage of our
452 experimental design is that all experiments were conducted in a simple low-variance
453 system by using a common crystal composition ($CaMgSi_2O_6$). This approach allows us
454 to evaluate the relative importance of crystal versus melt compositional effects on cpx–
455 melt partitioning under specific conditions.

456 The systematic relationship between Ds and ionic radii along the Onuma parabola
457 (Fig. 5) is a clear indication that the incorporation of trace elements into the crystal site
458 is controlled by cpx structural constituent. Previous studies have shown that ^{iv}Al and

459 Na content in cpx are the primary compositional variables in determining the cpx–melt
460 partition coefficient (e.g., Lundstrom et al., 1994; Skulski et al., 1994; Hill et al., 2000;
461 Bennett et al., 2004; Michely et al., 2017). The cpx crystals in this study are diopsidic
462 with variable Al_2O_3 and Na_2O contents, similar to those in equilibrium with basaltic
463 melts in many previous partitioning studies (e.g., Forsythe et al., 1994; Johnson, 1998;
464 Adam and Green, 2006). To evaluate and quantify the control of these variables on
465 FRTE and HFSE partitioning, our data were compared with these previous studies.

466 Tetrahedrally coordinated Al in cpx has been argued to increase *D*s for tri-, tetra-,
467 and pentavalent cations by providing a charge balancing mechanism for their
468 substitution into M site (e.g., Lundstrom et al., 1994; Gaetani and Grove, 1995; Hill et
469 al., 2000). For example, Wood and Trigila (2001) demonstrated that partition
470 coefficients increase by one order of magnitude for Ti and two orders of magnitude for
471 Zr, Nb, and Ta when the ^{iv}Al of cpx increases from 0.02 to 0.5. In this study, the Al_2O_3
472 contents in cpx range from 1.7 to 3.1 wt%, resulting in ^{iv}Al varying from 0.05 to 0.10
473 (p.f.u.). In Fig. 6, *D*s for Sc, Zr, Hf, and Nb are plotted against ^{iv}Al in cpx (see also Fig.
474 S5 for Cr, Ti, and Ta). To first order, D_{Cr} and all D_{HFSE} are systematically correlated with
475 ^{iv}Al within our new experimental dataset, supporting the ^{iv}Al as a control on highly
476 charged element partitioning. For Sc, this dependency is more subtle given the small
477 D_{Sc} range (3.62–6.35). Interestingly augite–basalt partitioning of Sc has been also
478 shown to be relatively constant, but rather dependent on experimental *T* (Dygert et al.,
479 2014). It is not surprising then that once the literature data is considered, the global
480 dataset might not be fitted with one universal trend, which may be expected given the

481 big gaps in melt compositions and experimental *P-T* conditions.

482 Sodium in cpx may also exert an important control on high-valence trace element
483 partitioning by increasing the charge-balanced configurations (Wood and Blundy 1997;
484 Blundy et al., 1998; Bennett et al., 2004). Bennett et al. (2004) performed experiments
485 in the NCMAS system and observed that the introduction of Na into cpx could lead to
486 an increase by at least three orders of magnitude for D_{HFSE} relative to those in the Na-
487 free system. Our study utilized both high- and low-Na compositions in the starting
488 materials, which produced a range of Na content in cpx (expressed in moles p.f.u., Na
489 = 0.035–0.067). However, as shown in Figs. 7 and S6, there is no indication that the Na
490 in cpx has any significant relationship with Sc, Cr, and HFSE partitioning. This can be
491 explained by the fact that our experiments were done with much less Na than achieved
492 by experiments in Bennett et al. (2004), in which a remarkable effect of Na in cpx has
493 only been observed for more Na-rich (2.2–13.5 wt% Na_2O) cpx at high-pressure
494 conditions.

495 In sum, the data examined in this study confirm that an ^{iv}Al-controlled substitution
496 mechanism for highly charged transition metal and HFSE partitioning extends to silicic
497 systems. When the results from these and other partitioning studies are compared (Figs.
498 6–7), it becomes apparent that the elevated partition coefficients in our experiments
499 cannot be reconciled by considering only the cpx composition. We would further argue
500 for a role of melt composition on FRTE and HFSE partitioning which is discussed in
501 the following section.

4.3. Effect of melt composition on D_{FRTE} and D_{HFSE}

It has long been recognized that melt composition influences the melt structure, and thus trace element *D*s, that generally increase with increasing melt polymerization (e.g., Ryerson and Hess, 1978; Mysen, 2004). Our new results, combined with those from previous studies, are useful for elucidating melt composition/structure controls on FRTE and HFSE partitioning. Basically, NBO/T has been widely used as an expression of the melt structure, and more specifically the degree of polymerization (with lower values indicating more polymerized melts; Mysen and Virgo, 1980; Mysen et al., 1985). Several studies have emphasized that the influence of melt structure becomes more effective when NBO/T < 0.49 (e.g., Gaetani, 2004; Huang et al., 2006; Mollo et al., 2016). Other studies showed that trace element partitioning depends on the major element components in melt (e.g., O'Neill and Eggins, 2002; Evans et al. 2008; Dygert et al., 2013). In this regard, Leitzke et al. (2016) observed that in basaltic systems, $D_{HFSE}^{cpx/melt}$ decreases with increasing TiO_2 in the melt. Some studies have also highlighted that the molar $Ca^{2+}/(M^{+} + M^{2+})$ of the melt, where M^{+} and M^{2+} are $Na^{+} + K^{+}$ and $Fe^{2+} + Ca^{2+} + Mg^{2+}$ cations, respectively, exerts a significant control on $D_{REE}^{cpx/melt}$ (Huang et al., 2006; Mollo et al., 2016). Furthermore, the global fit of cpx–melt partitioning data revealed that most *D*s increase as melt MgO, Mg#, CaO, and FeO contents drop, and as melt SiO_2 and $Na_2O + K_2O$ increase (Bédard, 2014).

Our dataset offers the opportunity to shed further light on these melt compositional effects. Taking into account of the structural environment of FRTE and HFSE in silicic melt (e.g., Schmidt et al., 2006), we investigate several melt variables that potentially

influence cpx–melt partitioning. In Figs. 8–10 we illustrate the variations in *D*s with different melt parameters (NBO/T, $Mg^{2+}/(M^{+} + M^{2+})$, ASI, and $Na_2O + K_2O$, respectively). It is noteworthy to mention that these variables are interrelated to some extent, so they cannot be considered exclusive of one another.

4.3.1. Partitioning of FRTE and HFSE as a function of NBO/T. In Fig. 8, partition coefficients for Co, Ni, Mn, Cu, Zn, Cr, Sc, Ti, Zr, Hf, Nb, and Ta from this study and the literature are plotted against NBO/T. Among the global dataset, in which cpx composition remains nearly constant (i.e., diopsidic with $^{iv}Al < 0.2$) over a range of NBO/T (0–1.2; Fig. 8), we are able to assess the isolated effect of melt composition. The systematic correlations of most *D*s and especially D_{Co}, D_{Ni}, and D_{Mn} with NBO/T are broadly consistent with previous work which established that the polymerization of melt influences remarkably the partitioning of high Z^{+}/r_i cations such as FRTE and HFSE (e.g., Ryerson and Hess, 1978; Schmidt et al., 2006). In detail, our new experimental data fall within or extend the trends established by the global dataset at the low NBO/T end of the distribution (Fig. 8). Moreover, in agreement with Gaetani (2004), we observe stronger dependence of the *D*s on NBO/T in more polymerized melts with NBO/T < 0.49 when compared to the cpx–basalt partitioning.

Although the partitioning data discussed above are consistent with a melt structural control, it has been pointed out in many previous studies that melt compositional effects are not fully captured by NBO/T (e.g., Bennett et al., 2004; Huang et al., 2006; Michely et al., 2017). Indeed, NBO/T treats structural role of individual M^{+} (Na^{+} and K^{+}) and M^{2+} (Mg^{2+}, Ca^{2+}, and Fe^{2+}) cations the same, and therefore does

546 not account for their fundamentally different behaviors in affecting melt structure (e.g.,
547 Mysen et al., 1985). The same is also likely true for some aspects of the NBO/T–*D*s
548 relationships in Fig. 8. For example, in light of our new data, D_{HFSE} does not increase
549 regularly with decreasing NBO/T from 0.22 to 0.1. As demonstrated, the highest D_{HFSE}
550 commonly shares a characteristic moderate NBO/T (e.g., maximum D_{Hf} at NBO/T =
551 0.15). Thus, the above considerations suggest that NBO/T is insufficient as a single melt
552 compositional term to describe the partitioning behavior of FRTE and HFSE in our
553 experiments.

554 **4.3.2. D_{FRTE} and melt $Mg^{2+}/(M^{+} + M^{2+})$.** Partition coefficients obtained in this
555 study confirm that, for a highly polymerized silicate melt with NBO/T < 0.2, small
556 changes in melt structure have a dramatic effect. While NBO/T cannot adequately
557 account for all subtleties in the strongly polymerized melt, a more subtle investigation
558 of the influence of melt structure on trace element partitioning is necessary. The
559 compositional changes in the melt among our experiments mostly reflect variation in
560 Mg, Ca, and total alkali content, depending on starting materials and the proportion of
561 crystals. Informed by the negative correlation of $D_{REE}^{cpx/melt}$ with melt molar $Ca^{2+}/(M^{+} +$
562 $M^{2+})$ in silicic systems (Huang et al., 2006), we test $Mg^{2+}/(M^{+} + M^{2+})$ as a potential melt
563 descriptor to account for the influence of melt structure on FRTE partitioning.
564 Rationally, transition metals with similar charge and size to Mg^{2+} are expected to show
565 more favorable incorporation into the melts with higher ratio of molar $Mg^{2+}/(M^{+} + M^{2+})$,
566 thereby reducing their partitioning into the crystalline phase. Besides, as our melts vary
567 in $Al_2O_3/(Na_2O + K_2O + CaO)$ with almost constant SiO_2 contents (Table 2), the ASI

parameter is used as an alternative indication of melt polymerization (Prowatke and Klemme, 2005).

Fig. 9 displays the relationships between D_{FRTE} with ASI (Fig. 9a-b) and $Mg^{2+}/(M^{+} + M^{2+})$ (Fig. 9c-d) for the experimental data reported here. It shows that, with the exception of Cu, Zn, and Sc showing small *D*s variations, partition coefficients of Co, Mn, Ni, and Cr are positively correlated with melt ASI. These well-defined trends agree well with the notion that minerals crystallized in the more strongly polymerized melts with higher ASI generally show increased *D*s, which is also well established in the literature (e.g., Prowatke and Klemme, 2005). On the other hand, *D*s of Co, Ni, and to a lesser extent Mn, show negative dependencies on melt $Mg^{2+}/(M^{+} + M^{2+})$, although the trends for the other transition metals are not clear enough to be definitive. These results strongly recall those of Huang et al. (2006) and further indicate a direct link between melt Mg and FRTE partitioning behavior. Such a causal relationship could be expected from the structural role of Mg in the melt.

Previous studies have suggested that the constitution of the melt network is governed by an equilibrium reaction (e.g., Stebbins, 1987): $2Q^{n} \leftrightarrow Q^{n-1} + Q^{n+1}$ (where Q^{n} denotes species in silicate melt with different numbers of bridging oxygen; $0 \leq n \leq 4$). The reaction shifts to the right as the charge density (i.e., Z^{+}/r_{i}) of the network-modifying cations increases (Maekawa et al., 1991; Mysen, 2004). Thus, as the Z^{+}/r_{i} increases with increasing $Mg^{2+}/(M^{+} + M^{2+})$ in the melt, the network tends to be less regular with both larger and smaller sites produced in the structure. This increase in the number of available sites would be critical for accommodating some transition metals

in the melt, resulting in lower *D*s. Particularly, the charge and ionic radius of both Co^{2+} and Ni^{2+} (in 6-fold coordination, 0.65 and 0.69 Å, respectively; Shannon, 1976) make it much easier to substitute for Mg^{2+} (0.72 Å in 6-fold coordination) than other mono- or divalent cations (e.g., Na^{+}, Ca^{2+}) in the melt, thus giving rise to the strong negative correlations between their *D*s and the melt $Mg^{2+}/(M^{+} + M^{2+})$.

4.3.3. D_{HFSE} and melt alkalis. Several previous studies have proposed that the effect of melt composition on mineral–melt *D*s is related to trace element solubility in silicate melts (e.g., Watson, 1979; O'Neill and Eggins, 2002; Bennett et al., 2004; Dygert et al., 2013; Michely et al., 2017). In this sense, the formation of melt complexes involving the trace element of interest and a major element in the melt, such as CaO (e.g., $CaMoO_3$ and $CaMoO_4$ complexes; O'Neill and Eggins, 2002), could change the activity coefficient of the trace element, thereby affecting its partitioning behavior. For HFSE, melt complexation with alkalis is thought to significantly affect its solubility in high-silica melts (e.g., Watson, 1979; Horng et al., 1999; Linnen and Keppler, 2002). For example, Watson (1979) demonstrated that Zr solubility in silicic melts increases with increasing alkali in excess of Al_2O_3 because of the formation of melt $Na_4Zr(SiO_4)_2$ and $K_4Zr(SiO_4)_2$ complexes.

The remarkable feature of the results presented here is that all HFSE partition coefficients depend on melt composition in a similar way, which are illustrated by the negative correlations between D_{HFSE} and melt total alkali ($Na_2O + K_2O$) contents (Fig. 10). These correlations indicate that some fundamental chemical properties of the melts governed by alkalis control the activity coefficients of HFSE. Indeed, other than Zr^{4+},

612 previous studies have also suggested that K^+ has a strong influence on enhancing the
613 solubilities (and lowering activity coefficients) of both Nb and Ta, which forms Nb^{+5}-
614 O-K and Ta^{+5}-O-K species in peralkaline SiO_2–K_2O–Al_2O_3 melts (Horng et al., 1999).
615 It follows that the strong negative dependencies of D_{HFSE} on melt total alkalis could be
616 interpreted as evidence for the formation of alkali–HFSE complexes in melts, which
617 enhances the solubility of HFSE and, consequently, leads to a decrease of their *D*s.
618 Alternatively, HFSE may act as network-formers and copolymerize with SiO_2 (e.g.,
619 Ti^{4+}, Zr^{4+}, and P^{5+} replace Si^{4+} in tetrahedral coordination; Ryerson, 1985) when the
620 silicic melts evolve towards more alkaline, explaining the negative dependencies of
621 D_{HFSE} on melt alkalis. A more definitive constraint on the HFSE partitioning must await
622 future detailed research on their structural environment in the melts of our compositions.
623

624 # 5. Implications

625 Mantle partial melting and metasomatism are two fundamental processes that have
626 contributed to the chemical heterogeneities of the Earth and play a key role in the
627 evolution of the lithosphere (e.g., Albarède, 1998; Lundstrom, 2000; Gao et al., 2004;
628 Yu et al., 2006; Kiseeva et al., 2013; Koppers et al., 2021). The most common approach
629 to quantifying melt extraction and metasomatic processes that occur in the lithospheric
630 mantle has been to use the partition coefficients between minerals and melts (silicate
631 and/or carbonate) and mineral compositions in mantle-derived xenoliths (e.g., Ionov,
632 2010; Kiseeva et al., 2017, 2018; Li et al., 2022).
633 This study extends previous experimental work constraining the partitioning and

634 extraction of trace elements during melting of the shallow mantle, which has been on
635 silicic, alkaline, aluminous systems (Huang et al., 2006). To address this aspect, our
636 experiments were performed at relatively low pressure and the cpx compositions
637 resemble those from natural depleted peridotite. We build upon our new partition
638 coefficient dataset, as well as comparison with previous work, to explore the extents to
639 which crystal versus melt compositions control FRTE and HFSE partitioning between
640 cpx and silicic melts. This discussion is particularly relevant to petrogenetic studies of
641 the interaction between silicic melt and peridotite that occurs in a variety of tectonic
642 settings, as has been documented by interstitial xenolith glasses (e.g., Xu et al., 1996;
643 Coltorti et al., 2000; Miller et al., 2012).

644 Our newly determined *D*s in silicic systems differ significantly from those in mafic
645 systems in two aspects. First, most trace elements exhibit considerably higher
646 compatibilities in cpx from silicic melts relative to those from more mafic melts (Figs.
647 3 and 8). Second, our results show marked variability in *D*s for a number of trace
648 elements (e.g., two-fold or greater variations for D_{Ni}, D_{Cr}, D_{Nb}, and D_{Ta}) within melt
649 compositions that are restricted to two-percent silica interval (67.6–69.1 wt% SiO_2).
650 We demonstrate that coupled substitution involving Al in the tetrahedral site is the
651 major charge balance mechanism by which the highly charged trace elements are
652 incorporated into the cpx. As for the Na-coupled substitution, the cpx compositions
653 seem not high enough in Na content for this mechanism to be significant.

654 Our findings in conjunction with literature data also highlight the strong influence
655 of melt composition/structure on FRTE and HFSE partition coefficients. With

increasing polymerization of the melt (i.e., lower NBO/T or higher ASI), D_{FRTE} and D_{HFSE} roughly increase to different extent. Moreover, we identified simple correlations between *D*s and a range of melt parameters (i.e., melt $Mg^{2+}/(M^{+}+M^{2+})$ and total alkali contents) for individual FRTE and HFSE, supporting the role of melt NBO species or complexing ligands in controlling the partitioning of these elements. The implication is that even very small changes in melt major-element compositions can greatly affect element partitioning in strongly polymerized silicic systems.

It should be further stressed that the effect of melt composition will not only affect the partitioning of trace elements between melt and cpx, but also additional minerals such as amphibole (Tiepolo et al., 2007), rutile (Schmidt et al., 2004), titanite (Prowatke and Klemme, 2005), and apatite (Prowatke and Klemme, 2006). Thus, in the context of melt-lithosphere interactions, elemental partition coefficients for mantle crystalline phases are expected to shift towards higher values in the presence of silica-rich liquids that react with peridotite. Of particular, our experimentally determined *D*s for Ti, Zr, REE, and Sr agree well with the partitioning between diopside and silicic glass in harzburgite xenoliths (PAT2-68 in Vannucci et al. 1998), indicating these results may be applicable to lithospheric melting. As such, this new experimental dataset is of interest for the further modeling of multi-step polybaric mantle melting and metasomatism, e.g., as has been proposed for the genesis of hump-shaped REE patterns in mantle cpx via the melting of a depleted spinel lherzolite source and subsequent equilibration with the melt enriched in SiO_2, Al_2O_3, and alkalis at shallower depth (Lundstrom, 2000; Huang et al., 2006).

678 # Acknowledgements

679 This work was funded by grants from the National Key R&D Program of China
680 (2016YFC0600404), the National Science Foundation of China (41173031, 41325011,
681 and 41373007), and State Key Laboratory of Isotope Geochemistry grants (SKLIG-KF-
682 12-05, SKLIG-KF-13-03) to Fang Huang. We would like to thank Xingchao Zhang for
683 help during some high-temperature experiments, Changming Xing for assistance with
684 electron microprobe analysis, Liang Li for help with some LA-ICP-MS analysis. We
685 are also grateful to Jean H. Bédard, Megan Holycross, Róbert Arató, and an anonymous
686 reviewer for their constructive comments that greatly improved this manuscript, and
687 associate editor Kate Kiseeva for her instructive editorial handling.

688

689

References

Adam, J. and Green, T. (2006) Trace element partitioning between mica-and amphibole-bearing garnet lherzolite and hydrous basanitic melt: 1. Experimental results and the investigation of controls on partitioning behaviour. Contributions to Mineralogy and Petrology, 152, 1-17.

Albarède, F. (1998) The growth of continental crust. Tectonophysics, 296, 1-14.

Baudouin, C., France, L., Boulanger, M., Dalou, C. and Devidal, J.-L. (2020) Trace element partitioning between clinopyroxene and alkaline magmas: parametrization and role of M1 site on HREE enrichment in clinopyroxenes. Contributions to Mineralogy Petrology, 175, 1-15.

Beard, C.D., van Hinsberg, V.J., Stix, J. and Wilke, M. (2019) Clinopyroxene/melt trace element partitioning in sodic alkaline magmas. Journal of Petrology, 60, 1797–1824.

Bédard, J.H. (2014) Parameterizations of calcic clinopyroxene—Melt trace element partition coefficients. Geochemistry, Geophysics, Geosystems, 15, 303-336.

Bennett, S., Blundy, J. and Elliott, T. (2004) The effect of sodium and titanium on crystal-melt partitioning of trace elements. Geochimica et Cosmochimica Acta, 68, 2335-2347.

Blundy, J. and Wood, B. (1994) Prediction of crystal melt partition coefficients from elastic moduli. Nature, 372, 452-454.

Blundy, J. and Wood, B. (2003) Partitioning of trace elements between crystals and melts. Earth and Planetary Science Letters, 210, 383-397.

Blundy, J.D., Robinson, J.A.C. and Wood, B.J. (1998) Heavy REE are compatible in clinopyroxene on the spinel lherzolite solidus. Earth and Planetary Science Letters, 160, 493-504.

Bonechi, B., Perinelli, C., Gaeta, M., Fabbrizio, A., Petrelli, M. and Strnad, L. (2021) High pressure trace element partitioning between clinopyroxene and alkali basaltic melts. Geochimica et Cosmochimica Acta, 305, 282-305.

Brice, J. (1975) Some thermodynamic aspects of the growth of strained crystals. Journal of Crystal Growth, 28, 249-253.

Cartier, C., Hammouda, T., Doucelance, R., Boyet, M., Devidal, J.-L. and Moine, B. (2014) Experimental study of trace element partitioning between enstatite and melt in enstatite chondrites at low oxygen fugacities and 5GPa. Geochimica et Cosmochimica Acta, 130, 167-187.

Coltorti, M., Beccaluva, L., Bonadiman, C., Salvini, L. and Siena, F. (2000) Glasses in mantle xenoliths as geochemical indicators of metasomatic agents. Earth and Planetary Science Letters, 183, 303-320.

Dalou, C., Boulon, J., T. Koga, K., Dalou, R. and Dennen, R.L. (2018) DOUBLE FIT: Optimization procedure applied to lattice strain model. Computers & Geosciences, 117, 49-56.

Draper, D.S. and Green, T.H. (1997) P–T phase relations of silicic, alkaline, aluminous mantle-xenolith glasses under anhydrous and C–O–H fluid-saturated conditions.

732 Journal of Petrology, 38, 1187-1224.
733 Draper, D.S. and Green, T.H. (1999) P–T phase relations of silicic, alkaline, aluminous
734 liquids: new results and applications to mantle melting and metasomatism. Earth
735 and Planetary Science Letters, 255-268.
736 Dunn, T. (1987) Partitioning of Hf, Lu, Ti, and Mn between olivine, clinopyroxene and
737 basaltic liquid. Contributions to Mineralogy Petrology, 96, 476-484.
738 Dygert, N., Liang, Y. and Hess, P. (2013) The importance of melt TiO2 in affecting
739 major and trace element partitioning between Fe–Ti oxides and lunar picritic glass
740 melts. Geochimica et Cosmochimica Acta, 106, 134-151.
741 Dygert, N., Liang, Y., Sun, C. and Hess, P. (2014) An experimental study of trace
742 element partitioning between augite and Fe-rich basalts. Geochimica et
743 Cosmochimica Acta, 132, 170-186.
744 Evans, T.M., O'Neill, H.S.C. and Tuff, J. (2008) The influence of melt composition on
745 the partitioning of REEs, Y, Sc, Zr and Al between forsterite and melt in the system
746 CMAS. Geochimica et Cosmochimica Acta, 72, 5708-5721.
747 Fedele, L., Zanetti, A., Morra, V., Lustrino, M., Melluso, L. and Vannucci, R. (2009)
748 Clinopyroxene/liquid trace element partitioning in natural trachyte–
749 trachyphonolite systems: insights from Campi Flegrei (southern Italy).
750 Contributions to Mineralogy Petrology, 158, 337-356.
751 Forsythe, L., Nielsen, R. and Fisk, M. (1994) High-field-strength element partitioning
752 between pyroxene and basaltic to dacitic magmas. Chemical Geology, 117, 107-
753 125.
754 Gaetani, G.A. (2004) The influence of melt structure on trace element partitioning near
755 the peridotite solidus. Contributions to Mineralogy Petrology, 147, 511-527.
756 Gaetani, G.A. and Grove, T.L. (1995) Partitioning of rare earth elements between
757 clinopyroxene and silicate melt Crystal-chemical controls. Geochimica et
758 Cosmochimica Acta, 59, 1951-1962.
759 Gao, S., Rudnick, R.L., Yuan, H.-L., Liu, X.-M., Liu, Y.-S., Xu, W.-L., Ling, W.-L.,
760 Ayers, J., Wang, X.-C. and Wang, Q.-H. (2004) Recycling lower continental crust
761 in the North China craton. Nature, 432, 892-897.
762 Guillong, M., Hametner, K., Reusser, E., Wilson, S.A. and Günther, D. (2005)
763 Preliminary Characterisation of New Glass Reference Materials (GSA-1G, GSC-
764 1G, GSD-1G and GSE-1G) by Laser Ablation-Inductively Coupled Plasma-Mass
765 Spectrometry Using 193 nm, 213 nm and 266 nm Wavelengths. Geostandards and
766 Geoanalytical Research, 29, 315-331.
767 Halicz, L. and Günther, D. (2004) Quantitative analysis of silicates using LA-ICP-MS
768 with liquid calibration. Journal of Analytical Atomic Spectrometry, 19, 1539-1545.
769 Hart, S.R. and Dunn, T. (1993) Experimental cpx/melt partitioning of 24 trace elements.
770 Contributions to Mineralogy Petrology, 113, 1-8.
771 He, Z., Huang, F., Yu, H., Xiao, Y., Wang, F., Li, Q., Xia, Y. and Zhang, X. (2016) A
772 flux-free fusion technique for rapid determination of major and trace elements in
773 silicate rocks by LA-ICP-MS. Geostandards and Geoanalytical Research, 40, 5-
774 21.
775 Hill, E., Blundy, J.D. and Wood, B.J. (2011) Clinopyroxene–melt trace element

partitioning and the development of a predictive model for HFSE and Sc. Contributions to Mineralogy Petrology, 161, 423-438.

Hill, E., Wood, B.J. and Blundy, J.D. (2000) The effect of Ca-Tschermaks component on trace element partitioning between clinopyroxene and silicate melt. Lithos, 53, 203-215.

Hirschmann, M.M., Baker, M.B. and Stolper, E.M. (1998) The Effect of Alkalis on the Silica Content of Mantle-Derived Melts. Geochimica et Cosmochimica Acta, 62, 883-902.

Holycross, M.E. and Bruce Watson, E. (2016) Diffusive fractionation of trace elements in basaltic melt. Contributions to Mineralogy Petrology, 171, 80.

Holycross, M.E. and Watson, E.B. (2018) Trace element diffusion and kinetic fractionation in wet rhyolitic melt. Geochimica et Cosmochimica Acta, 232, 14-29.

Holycross, M. and Cottrell, E. (2022) Experimental quantification of vanadium partitioning between eclogitic minerals (garnet, clinopyroxene, rutile) and silicate melt as a function of temperature and oxygen fugacity. Contributions to Mineralogy Petrology, 177, 21.

Horng, W.-S., Hess, P.C. and Gan, H. (1999) The interactions between M+5 cations (Nb+5, Ta+5, or P+5) and anhydrous haplogranite melts. Geochimica et Cosmochimica Acta, 63, 2419-2428.

Hou Z., Xiao Y., Shen J., Yu C. (2020) In situ rutile U-Pb dating based on zircon calibration using LA-ICP-MS, geological applications in the Dabie orogen, China. Journal of Asian Earth Sciences, 192, 104261.

Huang, F., Lundstrom, C. and McDonough, W. (2006) Effect of melt structure on trace-element partitioning between clinopyroxene and silicic, alkaline, aluminous melts. American Mineralogist, 91, 1385-1400.

Ionov, D.A. (2010) Petrology of Mantle Wedge Lithosphere: New Data on Supra-Subduction Zone Peridotite Xenoliths from the Andesitic Avacha Volcano, Kamchatka. Journal of Petrology, 51, 327-361.

Johnson, K.T. (1998) Experimental determination of partition coefficients for rare earth and high-field-strength elements between clinopyroxene, garnet, and basaltic melt at high pressures. Contributions to Mineralogy Petrology, 133, 60-68.

Kiseeva, E.S., Litasov, K.D., Yaxley, G.M., Ohtani, E. and Kamenetsky, V.S. (2013) Melting and Phase Relations of Carbonated Eclogite at 9–21 GPa and the Petrogenesis of Alkali-Rich Melts in the Deep Mantle. Journal of Petrology, 54, 1555-1583.

Kiseeva, E.S., Kamenetsky, V.S., Yaxley, G.M. and Shee, S.R. (2017) Mantle melting versus mantle metasomatism – “The chicken or the egg” dilemma. Chemical Geology, 455, 120-130.

Kiseeva, E.S., Vasiukov, D.M., Wood, B.J., McCammon, C., Stachel, T., Bykov, M., Bykova, E., Chumakov, A., Cerantola, V. and Harris, J.W. (2018) Oxidized iron in garnets from the mantle transition zone. Nature Geoscience, 11, 144-147.

Klein, M., Stosch, H.-G., Seck, H. and Shimizu, N. (2000) Experimental partitioning of high field strength and rare earth elements between clinopyroxene and garnet

in andesitic to tonalitic systems. Geochimica et Cosmochimica Acta, 64, 99-115.

Koppers, A.A.P., Becker, T.W., Jackson, M.G., Konrad, K., Müller, R.D., Romanowicz, B., Steinberger, B. and Whittaker, J.M. (2021) Mantle plumes and their role in Earth processes. Nature Reviews Earth & Environment, 2, 382-401.

Leitzke, F.P., Fonseca, R.O., Michely, L.T., Sprung, P., Münker, C., Heuser, A. and Blanchard, H. (2016) The effect of titanium on the partitioning behavior of high-field strength elements between silicates, oxides and lunar basaltic melts with applications to the origin of mare basalts. Chemical Geology, 440, 219-238.

Li, Y. (2018) Temperature and pressure effects on the partitioning of V and Sc between clinopyroxene and silicate melt: Implications for mantle oxygen fugacity. American Mineralogist, 103, 819-823.

Li, Y., Li, Y.-X. and Xu, Z. (2022) The partitioning of Cu and Ag between minerals and silicate melts during partial melting of planetary silicate mantles. Geochimica et Cosmochimica Acta, 324, 280-311.

Linnen, R.L. and Keppler, H. (2002) Melt composition control of Zr/Hf fractionation in magmatic processes. Geochimica et Cosmochimica Acta, 66, 3293-3301.

Liu, X., Xiong, X., Audétat, A. and Li, Y. (2015) Partitioning of Cu between mafic minerals, Fe-Ti oxides and intermediate to felsic melts. Geochimica et Cosmochimica Acta, 151, 86-102.

Liu, Y., Hu, Z., Gao, S., Gunther, D., Xu, J., Gao, C. and Chen, H. (2008) In situ analysis of major and trace elements of anhydrous minerals by LA-ICP-MS without applying an internal standard. Chemical Geology, 257, 34-43.

Luhr, J.F. and Carmichael, I.S. (1980) The colima volcanic complex, Mexico. Contributions to Mineralogy Petrology, 71, 343-372.

Lundstrom, C., Shaw, H., Ryerson, F., Phinney, D., Gill, J. and Williams, Q. (1994) Compositional controls on the partitioning of U, Th, Ba, Pb, Sr and Zr between clinopyroxene and haplobasaltic melts: implications for uranium series disequilibria in basalts. Earth and Planetary Science Letters, 128, 407-423.

Lundstrom, C., Shaw, H., Ryerson, F., Williams, Q. and Gill, J. (1998) Crystal chemical control of clinopyroxene-melt partitioning in the Di-Ab-An system: implications for elemental fractionations in the depleted mantle. Geochimica et Cosmochimica Acta, 62, 2849-2862.

Lundstrom, C.C. (2000) Rapid diffusive infiltration of sodium into partially molten peridotite. Nature, 403, 527-530.

Ma, S. and Shaw, C.S.J. (2021) An Experimental Study of Trace Element Partitioning between Peridotite Minerals and Alkaline Basaltic Melts at 1250°C and 1 GPa: Crystal and Melt Composition Impacts on Partition Coefficients. Journal of Petrology, 62, egab084.

Maekawa, H., Maekawa, T., Kawamura, K. and Yokokawa, T. (1991) Silicon-29 MAS NMR investigation of the sodium oxide-alumina-silica glasses. The Journal of Physical Chemistry, 95, 6822-6827.

Mallmann, G. and O'neill, H.S.C. (2009) The crystal/melt partitioning of V during mantle melting as a function of oxygen fugacity compared with some other elements (Al, P, Ca, Sc, Ti, Cr, Fe, Ga, Y, Zr and Nb). Journal of Petrology, 50,

1765-1794.

Michely, L., Leitzke, F., Speelmanns, I. and Fonseca, R. (2017) Competing effects of crystal chemistry and silicate melt composition on trace element behavior in magmatic systems: insights from crystal/silicate melt partitioning of the REE, HFSE, Sn, In, Ga, Ba, Pt and Rh. Contributions to Mineralogy Petrology, 172, 39.

Miller, C., Zanetti, A., Thöni, M., Konzett, J. and Klötzli, U. (2012) Mafic and silica-rich glasses in mantle xenoliths from Wau-en-Namus, Libya: Textural and geochemical evidence for peridotite–melt reactions. Lithos, 128-131, 11-26.

Miller, S.A., Asimow, P.D. and Burnett, D. (2006) Determination of melt influence on divalent element partitioning between anorthite and CMAS melts. Geochimica et Cosmochimica Acta, 70, 4258-4274.

Mollo, S., Forni, F., Bachmann, O., Blundy, J.D., De Astis, G., and Scarlato, P. (2016) Trace element partitioning between clinopyroxene and trachy-phonolitic melts: A case study from the Campanian Ignimbrite (Campi Flegrei, Italy). Lithos, 252-253, 160-172.

Mollo, S., Blundy, J., Scarlato, P., De Cristofaro, S.P., Tecchiato, V., Di Stefano, F., Vetere, F., Holtz, F., and Bachmann, O. (2018) An integrated P-T-H2O-lattice strain model to quantify the role of clinopyroxene fractionation on REE+Y and HFSE patterns of mafic alkaline magmas: Application to eruptions at Mt. Etna. Earth-Science Reviews, 185, 32-56.

Mollo, S., Blundy, J., Scarlato, P., Vetere, F., Holtz F., Bachmann, O., and Gaeta, M. (2020) A review of the lattice strain and electrostatic effects on trace element partitioning between clinopyroxene and melt: Applications to magmatic systems saturated with Tschermak-rich clinopyroxenes. Earth-Science Reviews, 210, 103351.

Mysen, B.O. (2004) Element partitioning between minerals and melt, melt composition, and melt structure. Chemical Geology, 213, 1-16.

Mysen, B.O. and Virgo, D. (1980) Trace element partitioning and melt structure: an experimental study at 1 atm pressure. Geochimica et Cosmochimica Acta, 44, 1917-1930.

Mysen, B.O., Virgo, D. and Seifert, F.A. (1985) Relationships between properties and structure of aluminosilicate melts. American Mineralogist, 70, 88-105.

Norman, M., Garcia, M.O. and Pietruszka, A.J. (2005) Trace-element distribution coefficients for pyroxenes, plagioclase, and olivine in evolved tholeiites from the 1955 eruption of Kilauea Volcano, Hawai'i, and petrogenesis of differentiated rift-zone lavas. American Mineralogist, 90, 888-899.

O'Neill, H.S.C. and Eggins, S.M. (2002) The effect of melt composition on trace element partitioning: an experimental investigation of the activity coefficients of FeO, NiO, CoO, MoO 2 and MoO 3 in silicate melts. Chemical Geology, 186, 151-181.

Onuma, N., Higuchi, H., Wakita, H., and Nagasawa, H. (1968) Trace element partition between two pyroxenes and the host lava. Earth and Planetary Science Letters, 5, 47-51.

Prowatke, S. and Klemme, S. (2005) Effect of melt composition on the partitioning of

trace elements between titanite and silicate melt. Geochimica et Cosmochimica Acta, 69, 695-709.

Prowatke, S. and Klemme, S. (2006) Trace element partitioning between apatite and silicate melts. Geochimica et Cosmochimica Acta, 70, 4513-4527.

Qian, Q., Hermann, J., Wang, Y., Guo, J., Liu, F. and Wang, L. (2015) Variations of clinopyroxene/melt element partitioning during assimilation of olivine/peridotite by low-Mg diorite magma. Chemical Geology, 419, 36-54.

Ryerson, F.J. (1985) Oxide solution mechanisms in silicate melts: Systematic variations in the activity coefficient of SiO2. Geochimica et Cosmochimica Acta, 49, 637-649.

Ryerson, F.J. and Hess, P.C. (1978) Implications of liquid-liquid distribution coefficients to mineral-liquid partitioning. Geochimica et Cosmochimica Acta, 42, 921-932.

Schmidt, M., Connolly, J., Günther, D. and Bogaerts, M. (2006) Element partitioning: the role of melt structure and composition. Science, 312, 1646-1650.

Schmidt, M.W., Dardon, A., Chazot, G. and Vannucci, R. (2004) The dependence of Nb and Ta rutile–melt partitioning on melt composition and Nb/Ta fractionation during subduction processes. Earth and Planetary Science Letters, 226, 415-432.

Schoneveld, L. and O'Neill, H.S.C. (2019) The influence of melt composition on the partitioning of trace elements between anorthite and silicate melt. Contributions to Mineralogy Petrology, 174, 13.

Shannon, R. D. (1976) Revised effective ionic radii and systematic studies of interatomic distances in halides and chalcogenides. Acta Crystallographica, A32, 751–767.

Skulski, T., Minarik, W. and Watson, E.B. (1994) High-pressure experimental trace-element partitioning between clinopyroxene and basaltic melts. Chemical Geology, 117, 127-147.

Stebbins, J.F. (1987) Identification of multiple structural species in silicate glasses by 29Si NMR. Nature, 330, 465-467.

Sun, C. and Liang, Y. (2012) Distribution of REE between clinopyroxene and basaltic melt along a mantle adiabat: effects of major element composition, water, and temperature. Contributions to Mineralogy Petrology, 163, 807-823.

Sun, C. and Liang, Y. (2013) The importance of crystal chemistry on REE partitioning between mantle minerals (garnet, clinopyroxene, orthopyroxene, and olivine) and basaltic melts. Chemical Geology, 358, 23-36.

Tiepolo, M., Oberti, R., Zanetti, A., Vannucci, R. and Foley, S.F. (2007) Trace-element partitioning between amphibole and silicate melt. Reviews in Mineralogy & Geochemistry, 67, 417-452.

Toplis, M.J. and Corgne, A. (2002) An experimental study of element partitioning between magnetite, clinopyroxene and iron-bearing silicate liquids with particular emphasis on vanadium. Contributions to Mineralogy Petrology, 144, 22-37.

Vannucci, R., Bottazzi, P., Wulff-Pedersen, E. and Neumann, E.-R. (1998) Partitioning of REE, Y, Sr, Zr and Ti between clinopyroxene and silicate melts in the mantle under La Palma (Canary Islands): implications for the nature of the metasomatic

952 agents. Earth and Planetary Science Letters, 158, 39-51.
953 Watson, E.B. (1976) Two-liquid partition coefficients: experimental data and
954 geochemical implications. Contributions to Mineralogy Petrology, 56, 119-134.
955 Watson, E.B. (1979) Zircon saturation in felsic liquids: experimental results and
956 applications to trace element geochemistry. Contributions to Mineralogy Petrology,
957 70, 407-419.
958 Watson, E.B. (1985) Henry's law behavior in simple systems and in magmas: Criteria
959 for discerning concentration-dependent partition coefficients in nature.
960 Geochimica et Cosmochimica Acta, 49, 917-923.
961 Wood, B.J. and Blundy, J.D. (1997) A predictive model for rare earth element
962 partitioning between clinopyroxene and anhydrous silicate melt. Contributions to
963 Mineralogy Petrology, 129, 166-181.
964 Wood, B.J. and Trigila, R. (2001) Experimental determination of aluminous
965 clinopyroxene–melt partition coefficients for potassic liquids, with application to
966 the evolution of the Roman province potassic magmas. Chemical Geology, 172,
967 213-223.
968 Xu, Y., Mercier, J.C.C., Lin, C., Shi, L., Menzies, M.A., Ross, J.V. and Harte, B. (1996)
969 K-rich glass-bearing wehrlite xenoliths from Yitong, Northeastern China:
970 petrological and chemical evidence for mantle metasomatism. Contributions to
971 Mineralogy Petrology, 125, 406-420.
972 Yaxley, G.M. and Kamenetsky, V. (1999) In situ origin for glass in mantle xenoliths
973 from southeastern Australia: insights from trace element compositions of glasses
974 and metasomatic phases. Earth and Planetary Science Letters, 172, 97-109.
975 Yu, J.-H., O'Reilly, S.Y., Zhang, M., Griffin, W.L. and Xu, X. (2006) Roles of Melting
976 and Metasomatism in the Formation of the Lithospheric Mantle beneath the
977 Leizhou Peninsula, South China. Journal of Petrology, 47, 355-383.
978 Yurimoto, H. and Sueno, S. (1987) Anion and cation partitioning between three
979 pyroxenes, chrome spinel phenocrysts and the host boninite magma: an ion
980 microprobe study. Geochemical Journal, 21, 85-104.

This is the peer-reviewed, final accepted version for American Mineralogist, published by the Mineralogical Society of America.
The published version is subject to change. Cite as Authors (Year) Title. American Mineralogist, in press.
DOI: https://doi.org/10.2138/am-2022-8586. http://www.minsocam.org/

981 **Table 1.** Major element (wt% oxides) compositions of starting materials, as measured by LA-ICP-MS under single-spot (30
982 μm) analytical mode.

Stating material	*n.*	SiO2	Al2O3	FeO	MgO	CaO	Na2O	K2O	TiO2	Cr2O3	Total
HISILA	8	68.2(1)	14.26(7)	1.65(3)	2.57(1)	3.49(7)	4.74(1)	3.84(2)	0.155(4)	0.053(3)	98.9
HISILB	8	67.5(1)	14.49(8)	1.65(1)	2.69(2)	3.38(7)	8.96(6)	–	0.115(3)	0.048(1)	98.9
HISILC	8	67.6(1)	14.28(10)	1.69(2)	2.63(3)	3.47(5)	8.9(1)	–	0.204(3)	0.077(1)	98.9
HISILA4D	8	67.9(3)	14.26(13)	1.76(5)	2.64(12)	3.56(17)	4.73(5)	3.85(4)	0.153(3)	0.062(3)	98.9
HISILA8D	7	67.7(3)	14.23(15)	1.73(3)	2.75(18)	3.69(29)	4.7(1)	3.91(9)	0.150(2)	0.065(2)	98.9

983 *Notes*: numbers in parentheses for this and subsequent tables indicate one standard deviation (1σ) of replicate analyses in terms of last significant
984 numbers: 68.2(1) should be read as 68.2 ± 0.1.
985

This is the peer-reviewed, final accepted version for American Mineralogist, published by the Mineralogical Society of America.
The published version is subject to change. Cite as Authors (Year) Title. American Mineralogist, in press.
DOI: https://doi.org/10.2138/am-2022-8586. http://www.minsocam.org/

986 **Table 2.** Major element (wt% oxides) compositions of glasses, as measured by LA-ICP-MS under single-spot (30 μm)
987 analytical mode.

Run #	1H04-1	2H04-2	3H04-3	4H04-4	5H05-1	6H05-2	7H05-3	8H07-1	9H07-2	10H08-1	11H08-2	12H09-1	13H09-2	14H09-3
Starting material	HISILA	HISILB	HISILA4D	HISILA8D	*HISILA	*HISILB	*HISILC	HISILB	HISILC	†HISILA	†HISILB	‡HISILA	‡HISILB	‡HISILC
n	12	10	10	13	10	10	11	11	15	13	13	10	12	10
SiO2 (wt%)	68.07(26)	68.21(42)	68.77(47)	69.11(43)	68.28(24)	67.59(34)	67.78(32)	68.87(21)	68.11(33)	68.55(45)	68.97(54)	68.42(48)	68.84(43)	69.01(53)
Al2O3	14.51(17)	14.89(27)	14.78(30)	15.27(28)	14.80(13)	14.65(26)	14.10(17)	14.88(22)	14.49(22)	14.93(29)	15.51(35)	14.84(28)	15.10(45)	14.90(32)
FeO	1.66(7)	2.11(13)	1.65(8)	1.54(3)	1.86(8)	1.75(5)	1.60(16)	1.62(4)	1.92(4)	1.94(7)	1.60(7)	1.66(5)	1.65(11)	1.67(11)
MgO	2.45(14)	2.26(34)	2.06(30)	1.38(8)	2.26(21)	2.46(17)	2.56(5)	1.83(10)	2.36(14)	1.91(16)	1.35(18)	2.34(8)	1.99(35)	1.81(22)
CaO	3.18(29)	2.30(25)	2.66(28)	2.40(9)	2.84(16)	3.03(25)	3.12(17)	2.43(19)	2.85(25)	2.55(16)	1.81(12)	2.84(26)	2.06(21)	2.31(31)
Na2O	4.79(6)	9.14(17)	4.88(6)	4.98(7)	4.86(4)	9.45(20)	9.41(11)	9.16(10)	8.95(9)	4.91(8)	9.44(17)	4.95(10)	9.22(16)	9.14(12)
K2O	4.02(10)		4.08(15)	4.21(8)	3.98(8)					3.95(11)		4.01(13)		
TiO2	0.159(4)	0.115(3)	0.162(5)	0.159(4)	0.164(3)	0.112(3)	0.198(5)	0.114(4)	0.198(4)	0.154(3)	0.116(4)	0.162(2)	0.115(2)	0.197(6)
Cr2O3	0.04(1)				0.024(2)	0.03(1)		0.03(1)	0.05(1)	0.02(1)		0.02(1)	0.02(1)	0.02(1)
MnO	0.047(2)	0.030(3)	0.039(6)	0.031(2)	0.048(3)	0.034(3)	0.059(3)	0.029(2)	0.055(5)	0.043(4)	0.029(3)	0.045(5)	0.031(4)	0.046(2)
SUM	98.93	99.04	99.08	99.08	99.12	99.10	98.82	98.97	98.99	98.95	98.83	99.30	99.04	99.10
ASI	0.81	0.77	0.86	0.89	0.85	0.69	0.66	0.76	0.72	0.88	0.82	0.84	0.80	0.78
Mg# (mole%)	72.4	65.7	69.1	61.5	68.4	71.5	74.0	66.8	68.7	63.7	60.1	71.5	68.2	65.9
$Mg^{2+}/(M^{+}+M^{2+})$	15.94	13.29	13.99	9.81	14.99	13.67	14.18	11.16	13.70	13.05	8.54	15.38	12.13	11.09
NBO/T	0.17	0.18	0.14	0.10	0.15	0.21	0.22	0.16	0.20	0.13	0.12	0.15	0.15	0.15

988

This is the peer-reviewed, final accepted version for American Mineralogist, published by the Mineralogical Society of America.
The published version is subject to change. Cite as Authors (Year) Title. American Mineralogist, in press.
DOI: https://doi.org/10.2138/am-2022-8586. http://www.minsocam.org/

989 **Table 3.** Major element (wt% oxides) compositions of cpx, as measured by EPMA.

Run #	1H04-1	2H04-2	3H04-3	4H04-4	5H05-1	6H05-2	7H05-3	8H07-1	9H07-2	10H08-1	11H08-2	12H09-1	13H09-2	14H09-3
Starting material	HISILA	HISILB	HISILA4D	HISILA8D	*HISILA	*HISILB	*HISILC	HISILB	HISILC	†HISILA	†HISILB	‡HISILA	‡HISILB	‡HISILC
n	7	9	4	9	8	8	8	5	6	5	5	6	7	7
SiO2 (wt%)	52.58(35)	53.86(25)	53.15(14)	53.19(55)	52.84(28)	53.66(25)	53.61(23)	53.78(19)	53.44(24)	52.65(8)	53.67(40)	52.75(22)	53.68(21)	53.22(18)
TiO2	0.10(1)	0.07(1)	0.096(4)	0.10(2)	0.12(2)	0.06(1)	0.13(1)	0.07(2)	0.12(2)	0.11(1)	0.07(1)	0.13(2)	0.07(2)	0.13(2)
Al2O3	2.59(21)	1.91(14)	2.66(24)	2.97(22)	3.09(16)	1.89(12)	1.83(15)	1.97(13)	1.88(10)	3.10(19)	1.70(9)	2.95(12)	2.09(11)	1.93(8)
FeO	2.13(8)	1.89(7)	2.24(15)	2.02(7)	2.52(14)	2.17(11)	2.12(9)	2.22(7)	1.98(3)	2.61(23)	2.21(9)	2.39(6)	2.27(10)	2.10(5)
MnO	0.08(1)	0.04(1)	0.10(01)	0.06(2)	0.09(1)	0.04(2)	0.08(1)	0.05(1)	0.08(2)	0.096(4)	0.05(2)	0.09(2)	0.05(2)	0.07(1)
MgO	18.50(22)	17.34(14)	18.33(37)	17.89(9)	18.35(15)	17.82(16)	17.40(14)	17.66(8)	17.48(11)	18.18(24)	17.60(7)	18.31(22)	17.59(18)	17.36(21)
CaO	21.32(20)	23.30(26)	21.72(61)	22.48(67)	21.16(56)	23.06(27)	23.02(27)	23.07(27)	22.56(26)	21.65(19)	22.83(24)	21.94(15)	22.70(41)	23.05(25)
K2O	0.05(2)		0.06(2)	0.04(1)	0.06(2)					0.05(1)		0.05(1)		
Na2O	0.49(2)	0.81(5)	0.51(3)	0.50(6)	0.53(6)	0.87(3)	0.88(6)	0.91(9)	0.93(4)	0.52(1)	0.90(5)	0.53(2)	0.95(4)	0.90(5)
NiO	0.44(2)	0.35(2)	0.36(2)	0.21(2)	0.44(2)	0.34(2)	0.53(3)	0.34(2)	0.57(2)	0.44(2)	0.29(2)	0.48(1)	0.30(4)	0.56(3)
Cr2O3	0.31(2)	0.22(1)	0.53(4)	0.21(4)	0.26(3)	0.12(2)	0.14(3)	0.17(4)	0.40(6)	0.23(3)	0.29(8)	0.28(6)	0.18(5)	0.30(6)
Total	98.60(33)	99.80(31)	99.76(48)	99.47(66)	99.46(49)	100.04(26)	99.71(32)	100.25(27)	99.45(34)	99.64(29)	99.61(34)	99.91(36)	99.89(30)	99.61(30)

990

This is the peer-reviewed, final accepted version for American Mineralogist, published by the Mineralogical Society of America.
The published version is subject to change. Cite as Authors (Year) Title. American Mineralogist, in press.
DOI: https://doi.org/10.2138/am-2022-8586. http://www.minsocam.org/

991 **Table 4.** Cpx–melt partition coefficients.

Run #	1H04-1	2H04-2	3H04-3	4H04-4	5H05-1	6H05-2	7H05-3	8H07-1	9H07-2	10H08-1	11H08-2	12H09-1	13H09-2	14H09-3
Starting material	HISILA	HISILB	HISILA4D	HISILA8D	*HISILA	*HISILB	*HISILC	HISILB	HISILC	†HISILA	†HISILB	‡HISILA	‡HISILB	‡HISILC
Si*	0.77(1)	0.79(1)	0.77(1)	0.77(1)	0.774(5)	0.79(1)	0.79(1)	0.781(4)	0.78(1)	0.77(2)	0.78(1)	0.77(2)	0.78(1)	0.77(1)
Al^{T*}	0.13(1)	0.08(1)	0.13(1)	0.12(1)	0.14(1)	0.11(1)	0.10(1)	0.11(1)	0.10(1)	0.15(1)	0.09(1)	0.15(1)	0.10(1)	0.11(1)
Al^{M1*}	0.049(4)	0.045(4)	0.054(5)	0.076(6)	0.072(4)	0.019(1)	0.030(2)	0.027(2)	0.030(2)	0.058(4)	0.022(1)	0.044(2)	0.039(2)	0.016(1)
Fe_{total}*	1.28(7)	0.90(6)	1.36(11)	1.31(5)	1.35(10)	1.24(7)	1.32(15)	1.36(5)	1.03(3)	1.35(13)	1.38(8)	1.44(6)	1.37(11)	1.26(9)
Fe_{total}	1.22(6)	1.05(15)	1.47(18)	1.47(13)	1.66(13)	1.16(19)	1.16(13)	1.36(14)	0.88(16)	1.19(20)	1.29(23)	1.45(14)	1.30(13)	1.30(27)
$Fe^{3+, M1*}$	1.28(7)	0.90(6)	1.27(10)	1.13(4)	1.19(9)	1.24(7)	1.32(15)	1.36(5)	1.03(3)	1.35(13)	1.38(8)	1.44(6)	1.37(11)	1.26(9)
Mg_{total}^{*}	7.55(45)	7.68(1.16)	8.88(1.29)	12.96(71)	8.10(76)	7.24(50)	6.80(14)	9.64(54)	7.41(45)	9.53(83)	13.01(1.74)	7.82(28)	8.84(1.54)	9.60(1.20)
Mg^{M1*}	6.60(39)	7.35(1.11)	7.82(1.13)	11.75(65)	6.99(65)	6.87(48)	6.48(14)	9.16(51)	6.97(42)	8.37(73)	12.32(1.65)	6.95(25)	8.32(1.45)	9.19(1.14)
Ca*	6.70(61)	10.14(1.11)	8.18(89)	9.36(44)	7.44(45)	7.61(62)	7.38(42)	9.48(74)	7.90(71)	8.50(52)	12.64(85)	7.71(70)	11.01(1.13)	10.00(1.34)
Na*	0.102(4)	0.088(6)	0.104(6)	0.101(13)	0.110(12)	0.092(4)	0.093(6)	0.100(10)	0.104(4)	0.106(3)	0.095(5)	0.108(4)	0.103(4)	0.098(5)
K*	0.013(4)		0.015(5)	0.010(4)	0.015(6)					0.0135(4)		0.013(3)		
Ti*	0.64(6)	0.63(11)	0.59(3)	0.64(10)	0.73(11)	0.56(9)	0.64(7)	0.59(16)	0.62(12)	0.71(7)	0.60(11)	0.82(10)	0.63(15)	0.67(9)
Ti	0.78(19)	0.77(13)	0.58(13)	0.72(12)	0.83(15)	0.57(12)	0.69(10)	0.63(34)	0.74(12)	0.81(15)	0.64(09)	0.73(17)	0.62(09)	0.71(14)
Cr*	8.46(1.58)				11.07(1.71)	4.44(1.16)		6.22(2.13)	8.44(1.63)	14.71(5.19)		13.62(4.88)	8.83(3.20)	11.97(4.01)
Cr	10.80(3.30)				13.19(2.24)	5.07(2.09)		10.22(3.66)	9.12(1.97)	19.01(7.17)		14.24(4.58)	11.77(4.65)	11.86(3.34)
Mn*	1.62(24)	1.33(35)	2.57(43)	1.94(71)	1.88(26)	1.25(51)	1.41(22)	1.74(47)	1.52(30)	2.24(21)	1.68(61)	2.05(44)	1.74(79)	1.58(24)
Mn	2.61(42)	2.34(35)	2.73(45)	2.96(61)	3.03(31)	1.99(31)	2.08(19)	2.54(49)	2.05(22)	3.72(47)	3.19(67)	2.84(44)	2.55(42)	2.85(41)
Ni*	13.88(2.40)	23.76(5.59)	28.00(6.82)	31.82(4.93)	20.30(1.63)	15.06(2.12)	12.79(1.58)	20.66(2.47)	15.77(2.10)	27.57(5.09)	34.02(3.80)	21.39(3.90)	24.68(5.97)	23.82(4.16)
Ni	14.41(3.10)	20.44(5.16)	18.23(5.58)	30.66(4.98)	21.15(3.00)	14.45(3.34)	12.56(2.90)	18.46(2.14)	15.35(2.30)	26.35(6.45)	40.21(6.80)	19.78(4.05)	26.49(6.01)	25.78(5.51)
Sc	3.99(45)	4.11(49)		5.17(85)	4.38(43)	3.62(47)	3.66(42)	5.56(79)	4.07(43)	5.29(1.20)	6.35(1.18)	4.90(1.00)	4.80(76)	5.34(45)
V	0.14(3)		0.108(4)			0.09(2)	0.12(4)	0.08(2)		0.10(3)	0.09(3)		0.07(1)	0.06(1)
Co	3.25(47)	3.31(45)	3.02(52)	4.46(84)	3.49(31)	2.76(44)	3.09(22)	3.96(57)	3.07(27)	4.14(70)	4.54(88)	3.61(49)	3.76(75)	3.91(30)
Cu			0.14(8)		0.33(11)	0.21(8)	0.16(1)		0.16(9)	0.37(6)		0.33(2)	0.21(8)	0.10(3)
Zn	1.04(11)		0.70(9)		0.94(9)	0.64(8)	0.60(5)	0.77(9)	0.60(5)	0.83(10)	0.79(12)	0.98(18)	0.85(14)	0.71(22)
Nb			0.03(1)		0.05(1)	0.03(1)	0.03(2)	0.02(1)	0.03(1)	0.04(2)	0.02(1)	0.03(1)	0.016(2)	0.011(3)
Ta			0.06(3)		0.08(2)	0.05(2)	0.04(2)	0.03(1)	0.07(1)	0.08(3)	0.05(2)	0.08(2)	0.04(1)	0.02(1)

This is the peer-reviewed, final accepted version for American Mineralogist, published by the Mineralogical Society of America.
The published version is subject to change. Cite as Authors (Year) Title. American Mineralogist, in press.
DOI: https://doi.org/10.2138/am-2022-8586. http://www.minsocam.org/

Zr	0.31(4)		0.18(8)		0.30(7)	0.21(4)	0.18(4)	0.21(4)	0.25(2)	0.31(5)	0.20(2)	0.31(5)	0.25(4)	0.28(5)
Hf	0.44(3)		0.33(3)		0.54(7)	0.36(6)	0.34(5)	0.36(11)	0.49(7)	0.53(12)	0.37(4)	0.63(6)	0.51(7)	0.53(10)
Rb	0.031(16)	0.099(26)	0.023(14)	0.122(38)	0.032(11)	0.027(15)	0.033(31)	0.009(11)	0.017(15)	0.034(22)	0.016(5)	0.019(3)	0.007(7)	0.008(6)
Sr	0.16(1)		0.19(3)		0.20(5)	0.27(4)	0.26(3)	0.25(7)	0.27(3)	0.18(2)	0.33(3)	0.18(4)	0.29(4)	0.30(5)
La	0.26(5)		0.36(6)		0.29(3)	0.35(6)	0.40(8)	0.33(6)	0.40(5)	0.30(4)	0.39(5)	0.34(6)	0.39(8)	0.39(4)
Ce	0.38(2)		0.56(13)		0.49(6)	0.50(5)	0.51(5)	0.43(3)	0.50(3)	0.46(4)	0.57(11)	0.57(8)	0.53(11)	0.50(9)
Nd	0.88(7)	1.17(13)	0.94(12)	1.02(10)	1.15(8)	1.07(15)	0.94(10)	1.14(15)	1.12(11)	0.95(16)	1.23(11)	1.29(19)	1.23(18)	1.20(11)
Sm	1.69(13)		1.54(25)	1.65(21)	2.04(16)	1.31(15)	1.36(15)	1.93(27)	1.87(11)	1.94(20)	2.07(35)	2.00(19)	1.95(24)	2.01(21)
Eu	1.77(10)		1.72(31)	1.82(28)	2.15(18)	1.58(16)	1.54(12)	1.91(28)	1.73(17)	1.94(31)	2.22(48)	2.18(20)	2.13(33)	2.25(25)
Gd	1.71(16)	1.63(22)		1.70(14)	1.87(22)	1.49(21)	1.42(19)	2.08(16)	1.60(21)		2.05(16)	2.01(34)	2.04(30)	2.44(20)
Tb	1.69(43)	1.55(18)		1.69(19)	2.08(16)	1.54(19)	1.63(18)	2.04(25)	1.78(12)	1.95(32)	2.13(21)	2.19(14)	2.12(27)	2.56(33)
Dy			1.75(29)	1.75(26)	2.47(22)	1.48(20)	1.43(16)	2.09(28)	1.94(12)	1.96(27)	2.22(21)	2.23(20)	2.19(31)	2.15(23)
Ho	1.90(8)	1.68(19)	1.60(26)	1.76(26)	2.26(17)	1.49(13)	1.52(17)	2.04(15)	1.76(11)	1.90(27)	2.06(17)	2.23(20)	1.90(24)	2.23(27)
Er	1.92(36)	1.68(17)	1.41(14)	1.82(25)	2.40(17)	1.56(16)	1.66(22)	2.12(29)	1.64(7)	2.02(28)	2.01(14)	2.41(9)	1.97(24)	1.99(18)
Yb	1.67(8)	1.51(12)	1.31(17)	1.51(24)	2.15(27)	1.30(20)	1.27(26)	1.65(26)	1.57(17)	1.93(37)	1.94(13)	2.27(15)	1.82(28)	1.68(32)
Lu	1.65(16)	1.47(17)	1.44(16)	1.53(23)	2.08(13)	1.19(21)	1.08(14)	1.41(22)	1.54(16)	1.55(19)	1.54(10)	1.85(16)	1.55(16)	1.65(24)

992 Si*: Partition coefficients calculated from EPMA analyses of cpx. All other partition coefficients were calculated based on LA-ICP-MS data.

This is the peer-reviewed, final accepted version for American Mineralogist, published by the Mineralogical Society of America.
The published version is subject to change. Cite as Authors (Year) Title. American Mineralogist, in press.
DOI: https://doi.org/10.2138/am-2022-8586. http://www.minsocam.org/

Figures and captions

Fig. 1

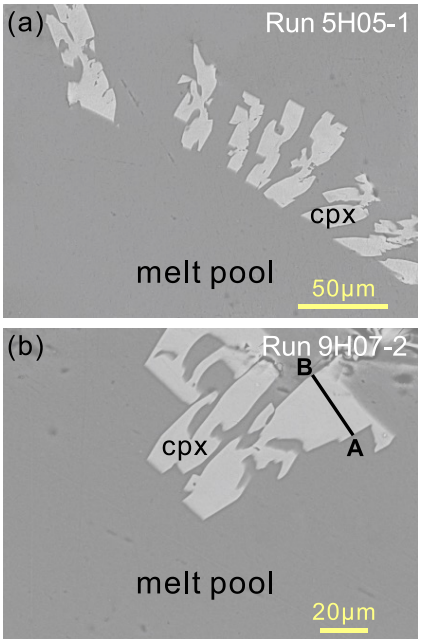

Fig. 1. Back-scattered electron images of experimental products in representative runs (a) 5H05-1 and (b) 9H07-2 showing euhedral-subhedral cpx coexisting with melt. The experimental charge has large melt pools free of microcrystals allowing micro-beam analyses. The line A–B in panel b represents the analytical traverse shown in Figure 4. Note that the dark area near the crystal is due to a polishing problem.

This is the peer-reviewed, final accepted version for American Mineralogist, published by the Mineralogical Society of America.
The published version is subject to change. Cite as Authors (Year) Title. American Mineralogist, in press.
DOI: https://doi.org/10.2138/am-2022-8586. http://www.minsocam.org/

1005 **Fig. 2**

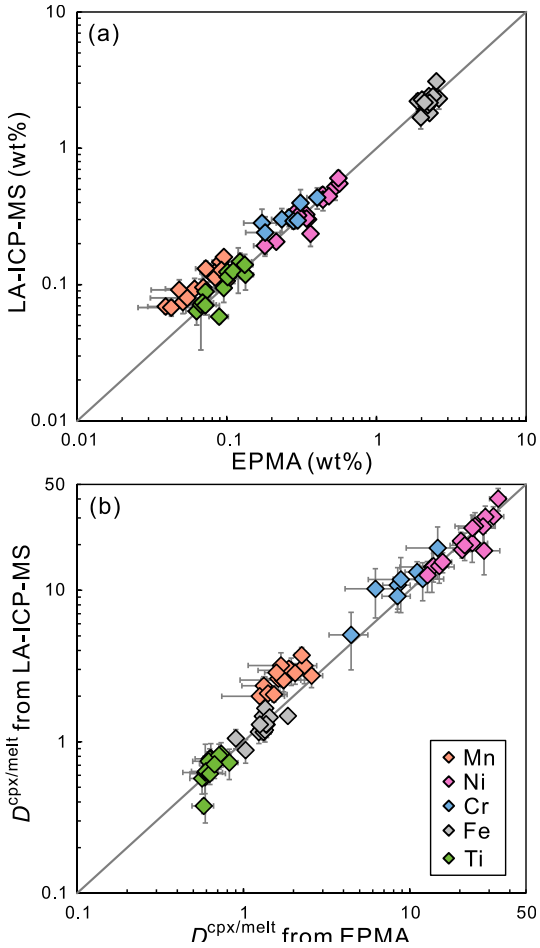

1006
1007

1008 **Fig. 2.** Comparison between EPMA and LA-ICP-MS analyses of MnO, NiO, Cr_2O_3,
1009 FeO_t, and TiO_2 concentrations for (a) cpx and (b) corresponding partition coefficients.
1010 Error bars on this and subsequent diagrams represent one standard deviation (1σ). The
1011 plots demonstrate very good agreement between the two analytical techniques. The
1012 solid grey line is the 1:1 ratio line.
1013

This is the peer-reviewed, final accepted version for American Mineralogist, published by the Mineralogical Society of America.
The published version is subject to change. Cite as Authors (Year) Title. American Mineralogist, in press.
DOI: https://doi.org/10.2138/am-2022-8586. http://www.minsocam.org/

1014 **Fig. 3**

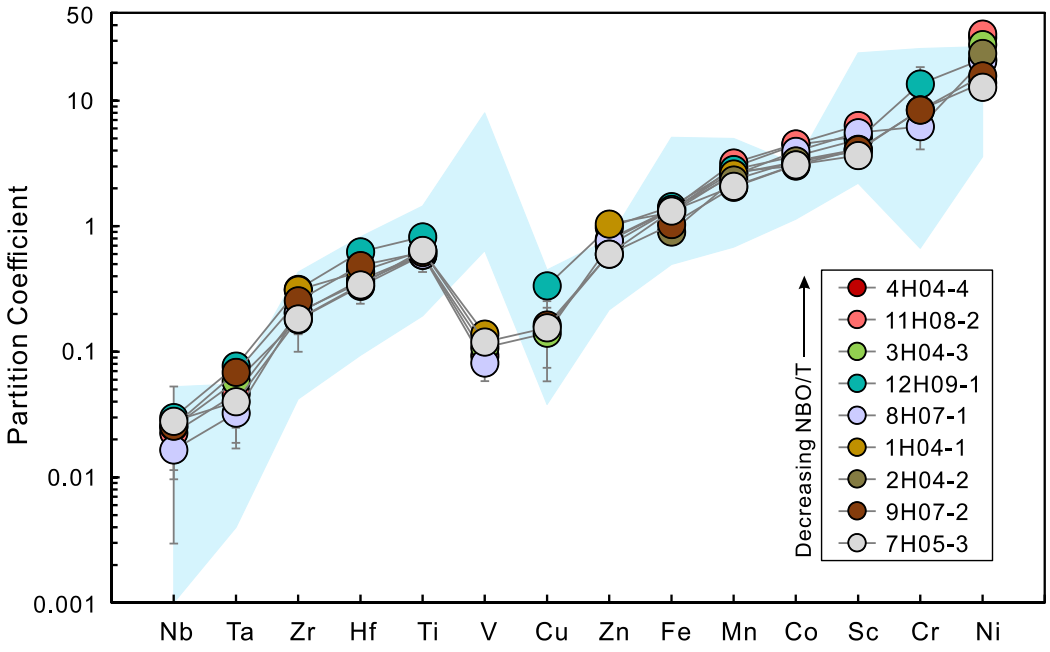

1015
1016

1017 **Fig. 3.** Cpx–melt FRTE and HFSE partition coefficient patterns obtained from nine
1018 representative runs with a range of melt NBO/T (0.10–0.22) in this study. The
1019 partitioning data from the literature (Luhr and Carmichael, 1980; Dunn, 1987; Yurimoto
1020 and Sueno, 1987; Forsythe et al., 1994; Skulski et al., 1994; Johnson, 1998; Toplis and
1021 Corgne, 2002; Norman et al., 2005; Adam and Green, 2006; Huang et al., 2006; Fedele
1022 et al., 2009; Liu et al., 2015), filtered based on diopsidic cpx with $^{iv}Al < 0.20$, are shown
1023 as blue shaded field for comparison.

1024

This is the peer-reviewed, final accepted version for American Mineralogist, published by the Mineralogical Society of America.
The published version is subject to change. Cite as Authors (Year) Title. American Mineralogist, in press.
DOI: https://doi.org/10.2138/am-2022-8586. http://www.minsocam.org/

Fig. 4

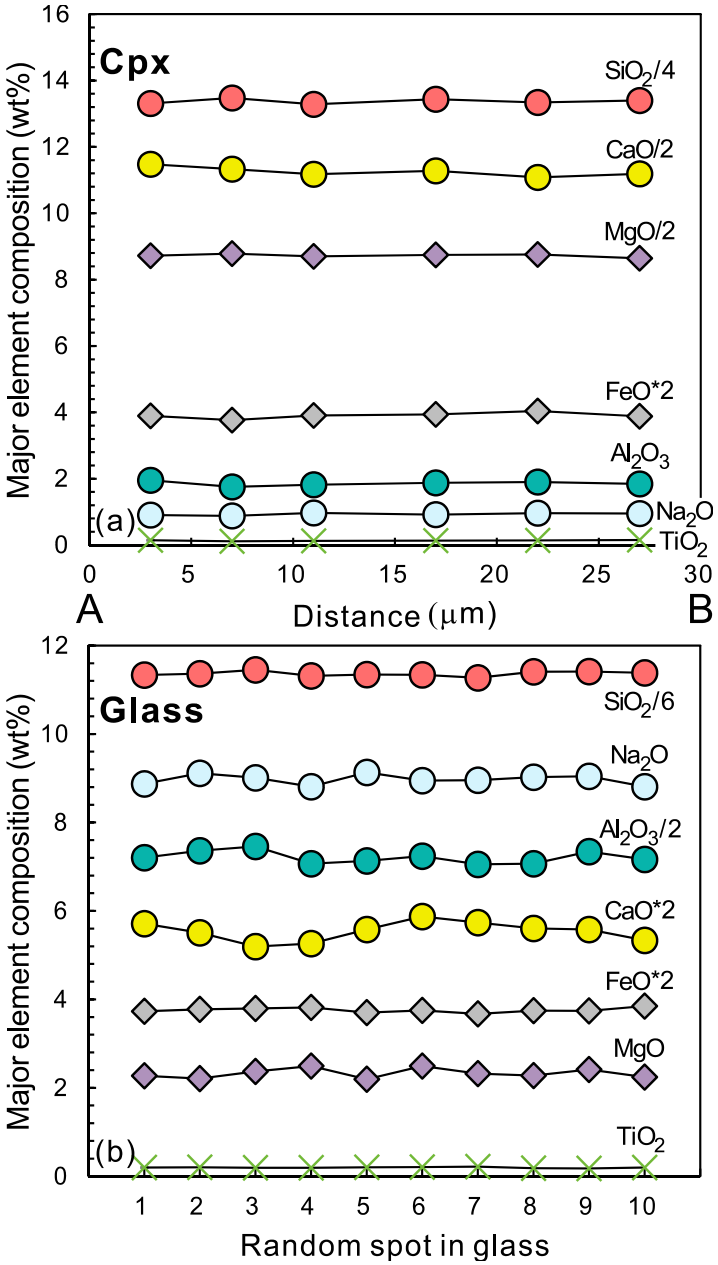

Fig. 4. Profiles of major-element compositional variations in clinopyroxene and glass. (a) Variation in composition of clinopyroxene across the analytical traverse A–B in Figure 1, showing minor zoning in major elements. (b) Variation in glass composition among 10 random spots. No variations outside of analytical errors are detectable.

Fig. 5

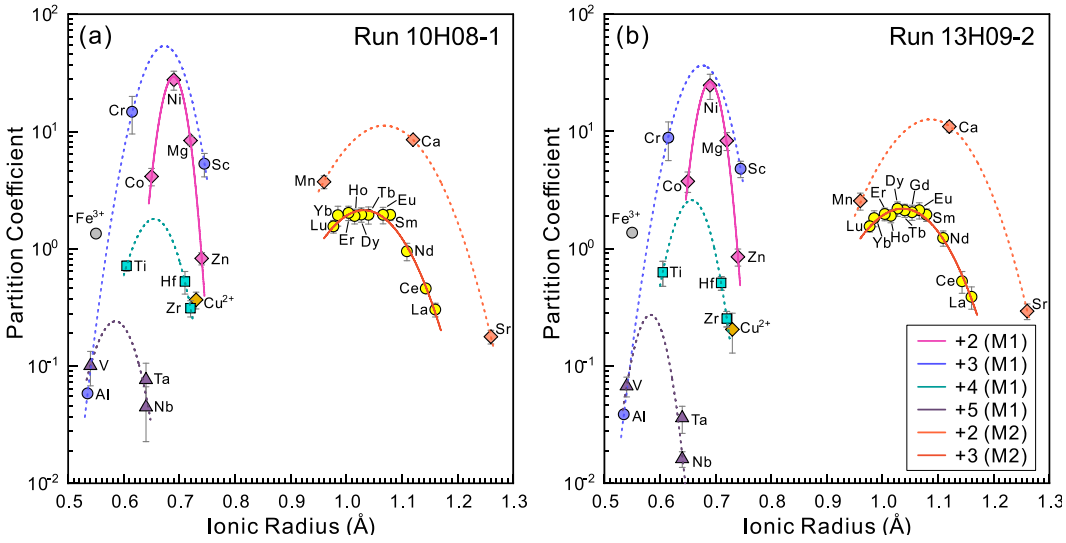

Fig. 5. Onuma diagrams showing partition coefficients for di-, tri-, tetra-, and pentavalent cations between cpx and melt as a function of ionic radii (in Å; Shannon, 1976). Ionic radii in VI- and VIII-fold coordination are taken for cations on the M1 and M2 site, respectively. The partitioning data are from two runs (a)10H08-1 and (b) 13H09-2 reported in this study. Color-coded curves represent least-squares fits of the data to the lattice strain model of Blundy and Wood (1994) as expressed in Eq. (1). Lattice strain parameter for tri-, tetra-, and pentavalent cations on the M1 site and divalent cations on the M2 site are unconstrained, thus parabolas are shown as dashed curves. For the fitting of trivalent cations on M1 site, D_{Al} on the M1 site was calculated as the difference between total Al and the ^{iv}Al partitioning into the tetrahedral site. Note that Cu^{2+} and Fe^{3+} were excluded from the fitting since they fall outside the parabolas defined by divalent and trivalent cations, respectively.

This is the peer-reviewed, final accepted version for American Mineralogist, published by the Mineralogical Society of America.
The published version is subject to change. Cite as Authors (Year) Title. American Mineralogist, in press.
DOI: https://doi.org/10.2138/am-2022-8586. http://www.minsocam.org/

Fig. 6

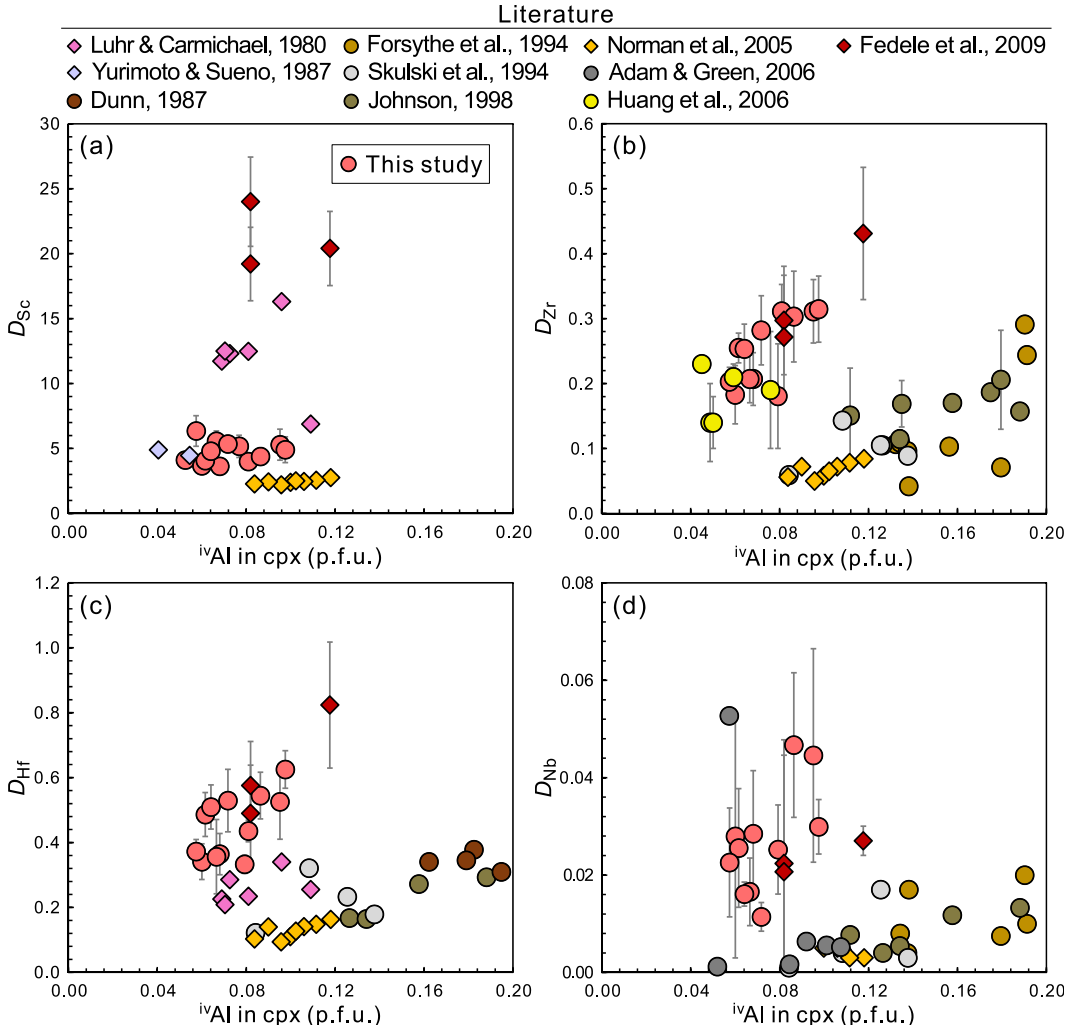

Fig. 6. Partition coefficients of (a) Sc, (b) Zr, (c) Hf, and (d) Nb between cpx and melt as a function of ^{iv}Al content (p.f.u. = per formula unit, calculated for six oxygens) of the cpx. Other partition coefficients for diopsidic cpx with ^{iv}Al < 0.2 from the literature are shown for comparison.

1055 **Fig. 7**

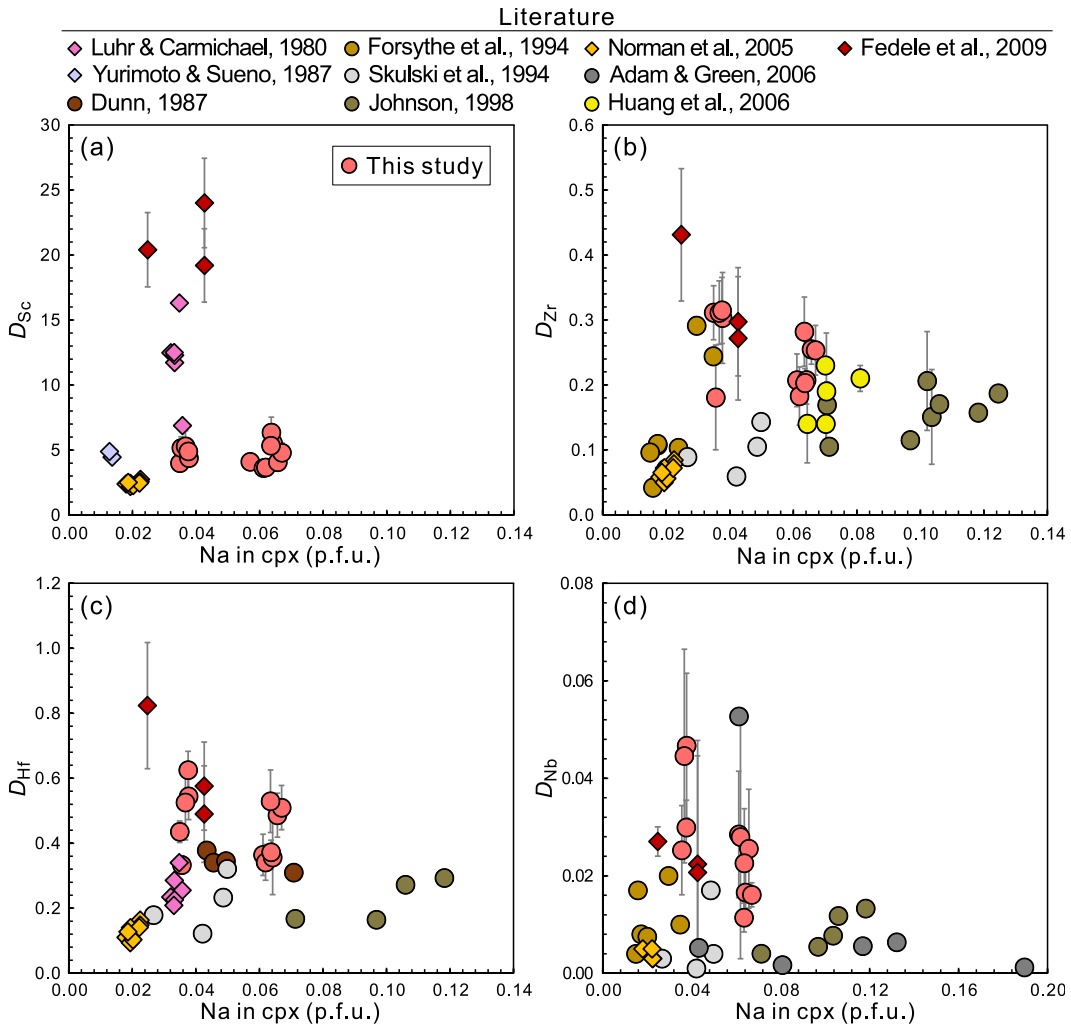

1056

1057 **Fig. 7.** Partition coefficients of (a) Sc, (b) Zr, (c) Hf, and (d) Nb between cpx and melt
1058 as a function of Na content (p.f.u.) of the cpx. Other partition coefficients for diopsidic
1059 cpx with $^{iv}Al < 0.2$ from the literature are shown for comparison.

This is the peer-reviewed, final accepted version for American Mineralogist, published by the Mineralogical Society of America.
The published version is subject to change. Cite as Authors (Year) Title. American Mineralogist, in press.
DOI: https://doi.org/10.2138/am-2022-8586. http://www.minsocam.org/

Fig. 8

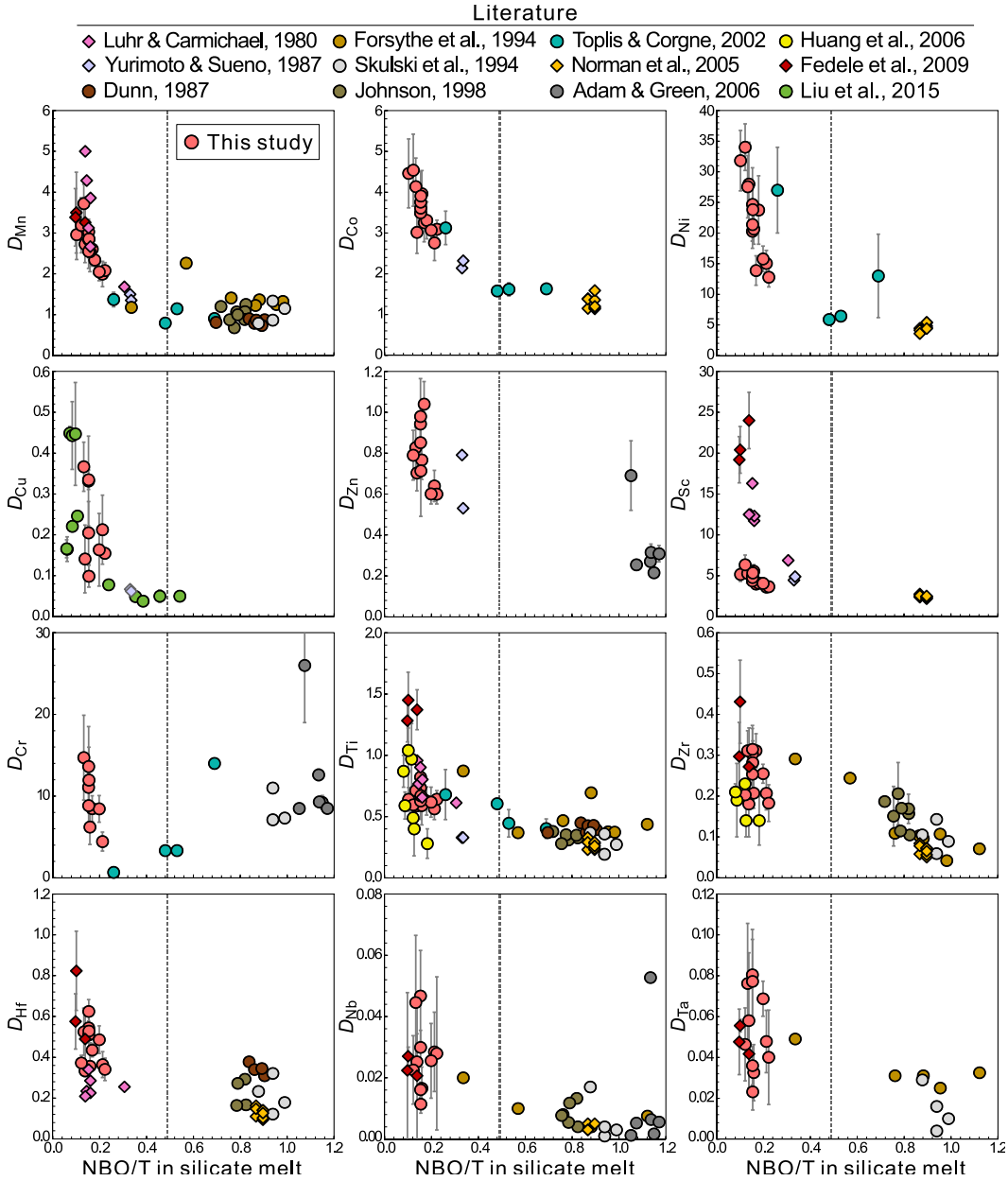

Fig. 8. Partition coefficients of Mn, Co, Ni, Cu, Zn, Sc, Cr, Ti, Zr, Hf, Nb, and Ta between cpx and melt as a function of NBO/T of the melt. In a completely polymerized melt NBO/T = 0, and in a completely depolymerized melt NBO/T = 4. The dashed gray vertical line corresponds to NBO/T = 0.49; at lower NBO/T values, melt structure significantly influences trace element partitioning (Gaetani 2004). Other partition coefficients for diopsidic cpx with $^{iv}Al < 0.2$ from the literature are shown for comparison.

This is the peer-reviewed, final accepted version for American Mineralogist, published by the Mineralogical Society of America.
The published version is subject to change. Cite as Authors (Year) Title. American Mineralogist, in press.
DOI: https://doi.org/10.2138/am-2022-8586. http://www.minsocam.org/

Fig. 9

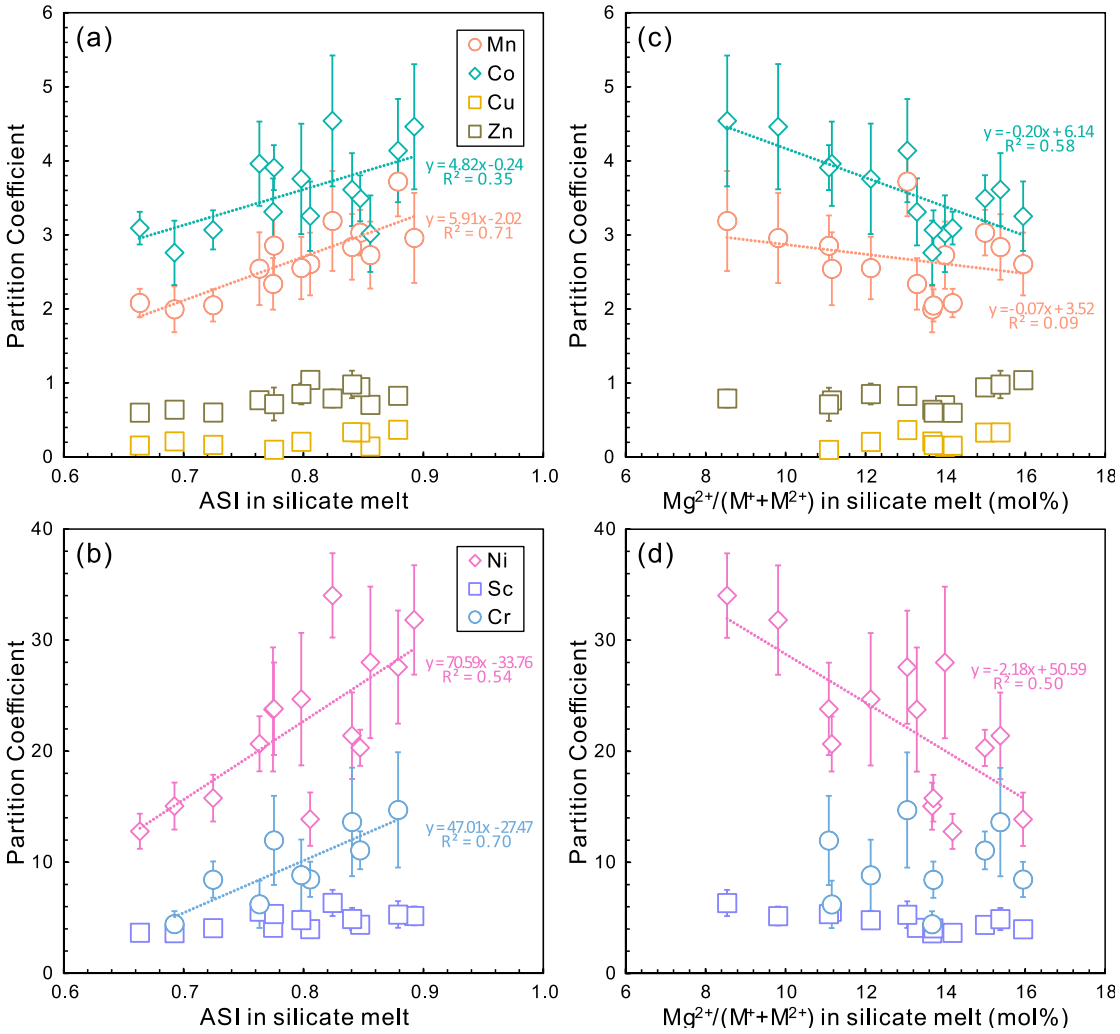

Fig. 9. Partition coefficients of Mn, Co, Cu, Zn, Ni, Sc, and Cr between cpx and melt as a function of (a-b) ASI and (c-d) $Mg^{2+}/(M^{+}+M^{2+})$ (mol%) of the melt.

This is the peer-reviewed, final accepted version for American Mineralogist, published by the Mineralogical Society of America.
The published version is subject to change. Cite as Authors (Year) Title. American Mineralogist, in press.
DOI: https://doi.org/10.2138/am-2022-8586. http://www.minsocam.org/

1075 **Fig. 10**

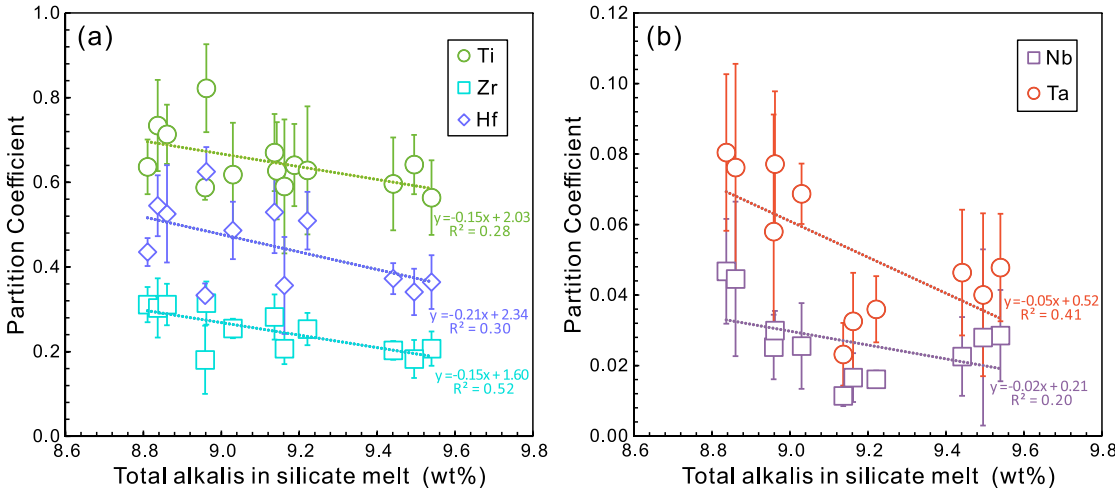

1076

1077 **Fig. 10.** Partition coefficients of (a) Ti, Zr, Hf, and (b) Nb and Ta between cpx and melt
1078 as a function of total alkalis ($Na_2O + K_2O$, wt%) of the melt.